Politecnico di Torino

Master's degree in biomedical engineering

Politecnico
di Torino

Development of a subject-specific finite element model of the thoracolumbar spine segment integrating CT and MRI images

Supervisor:
Dott.ssa Alessandra Aldieri

Prof.ssa Cristina Bignardi

Candidate:
Alessio Paolini

Academic Year 2024/25

Abstract

Finite Element Analysis (FEA) is an essential tool in biomedical engineering and particularly in spinal biomechanics research. Subject-specific spine models provide a more realistic representation of load transmission, especially when there are structural changes involved, such as disc degeneration, a pathology strongly associated with chronic low back pain and mechanical instability. Under such a circumstance, it is paramount to include in the model, besides bone anatomy, the mechanical characterization of the intervertebral discs that is afforded by MRI images. The aim of this thesis is the creation of a three-dimensional patient-specific thoraco-lumbar spine model, developed from computed tomography (CT) and magnetic resonance imaging (MRI). CT images were used for segmentation and assignment of mechanical properties of vertebrae, whereas MRI was used to explore the morphology and segmentation of tissue properties of the IVDs. The integration of the two imaging modalities enabled the development of a 3D model that encompasses both anatomical accuracy and physiologic tissue response. MRI was utilized not only for morphological segmentation, but also for quantitative measurement of internal disc parameters such as water content and degeneration, which are not inferable from CT. The developed process involved semi-automatic segmentation of vertebrae in CT scans and intervertebral discs from MRI images using the 3D Slicer software. CT segmentations of the vertebras were, also, aligned to MRI reference space using an Iterative Closest Point (ICP) algorithm. The T9–T10 and T12–L1 discs, which were healthier, were separately segmented to distinguish the nucleus pulposus (NP) and annulus fibrosus (AF), whereas the T10–T11 and T11–T12 discs, which were degenerated, were modelled as homogeneous structures. For each segmented structure, T2 relaxation time was estimated using a Simulated Annealing optimization algorithm. T2 values were then used to estimate, through calibration curves, the water content and mechanical properties of the nucleus (elastic modulus and Poisson's ratio). The annulus fibrosus was modelled as a hyperelastic material using the Mooney–Rivlin formula. Where the nucleus could not be differentiated in the degenerated discs, the entire disc was regarded as AF, and the Mooney–Rivlin constants C1 and C2 were determined based on percentage disc height loss. The results indicate that T2 values correlate with the degree of degeneration: increased values in fewer degenerated discs, and lower degeneration values in degenerated discs. The elastic modulus of the nucleus increased while water content reduced, and the Poisson’s ratio reduced, indicating decreasing

volumetric deformability. C1 and C2 parameters were larger in strongly height-loss discs, since it indicates more stiff mechanical behaviour of the fibrous tissue. Overall, this study offers a comprehensive and reproducible workflow for spine biomechanical modelling using CT and MRI data for personalized assignment of disc material properties. The resulting model presents a solid basis for future FEM simulations regarding intervertebral disc degeneration.

Contents

List of Figures

List of tables

Abbreviations

Abbreviations	Meaning
AF	Annulus Fibrosus
BMU	bone mineral density
CT	Computed Tomography imaging
E	Elastic modulus
FEM	Finite element modelling
FIESTA	Fast Imaging Employing Steady-State Acquisition
FSU	Functional Spinal Units
HU	Hounsfield Units
B	compressibility
IVD	Intervertebral Disc
MRI	Magnetic Resonance Imaging
NP	Nucleus Pulposus
TE	Echo Time
SI	Signal Intensity
%W:C	Percentual of water content

Chapter 1.

Introduction

1.1 Theoretical Background

In this chapter, the anatomical and biomechanical characteristics of the spinal column will be studied in detail, with particular focus on the thoracic and lumbar region. After a description of the primary components of the spinal column - vertebrae, intervertebral discs, biomechanical behaviour will be studied, focusing on how it arises from the physiological characteristics of the underlying structures.

1.2 Anatomy of spinal column.

Spinal column, or spine, is among the most critical elements of the human skeleton. Spine performs numerous functions like bearing body weight, encasing the spinal cord, and helping head and trunk movements. Spine anatomically extends from the head to the top of coccyx, and it is made up of 33 or 34 bones segments known as vertebrae. (Figure1 [1]).

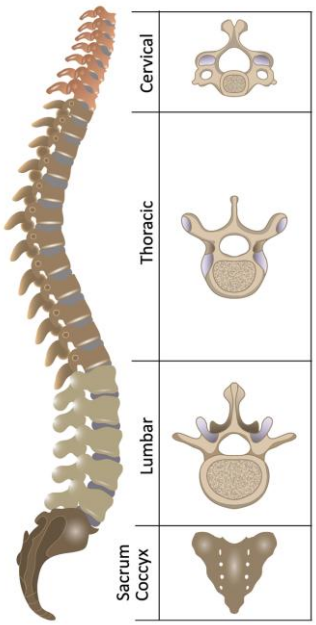

Figure 1:Anatomy of the spine collum

It is divided into the five individual regions: cervical (7 vertebrae), thoracic (12 vertebrae), lumbar (5 vertebrae), sacral (5 fused vertebrae to form the sacrum), coccygeal (4-5 fused

vertebrae to form the coccyx). All the regions serve different roles and possess different anatomical features based on where they are located in the body [2].

Spinal column is not vertical but consists of a series of lateral curves both in the frontal and sagittal planes. Two posterior concavity curves, cervical and lumbar lordosis, and two anterior concavity curves, thoracic and sacral kyphosis, laterally. Kyphoses are also called primary or accommodation curvatures as they accommodate the abdominal and thoracic viscera, while the lordoses, or secondary or compensation curves, aid in the accommodation of the head and body weight. The transition from one to the other curve is progressive except during sudden transition from lumbar lordosis to sacral kyphosis that results in the formation of the sacral promontory of the base of the sacral base. Simply put, it can be stated that the spine has the same configuration of two 'S' upon each other. The vertebrae become broader as one progresses from the superior to the caudal area, since lower vertebrae need to bear a progressively greater load.[3]

1.3 Vertebral Anatomy and Function

Vertebrae are classified as short bones; they are made up largely of spongy bone supported by a thin layer of compact bone. Even though each vertebra has unique features that identify it with certain parts of the spine, general anatomic elements can be established so an average vertebra can be described. At the front, each vertebrae have a thick and cylindrical in shape body whose purpose is to spread weight along the backbone. The vertebral body consists of a spongy centre surrounded by a ring of dense bone peripherally. Its superior surface articulates with the inferior surface of the upper vertebra; both surfaces are slightly concave in the centre and convex at the margins so that a disc of cartilaginous tissue known as IVDs can fit in (Figure 2 [4])

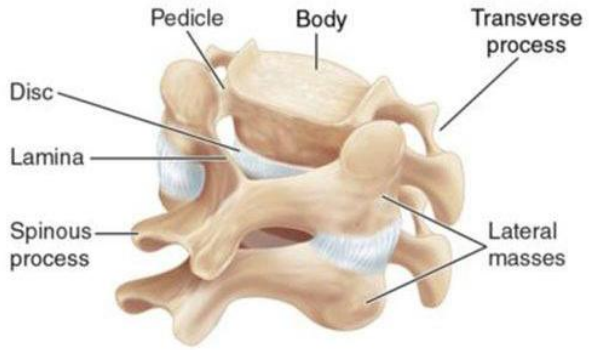

Figure 2: Anatomy of the vertebrae

Posteriorly the vertebral arch or neural arch projects from the vertebral body and defines the margins of the neural hole.[3]. Vertebral arch is limited by posterior surface of vertebral body, pedicles and laminae. Pedicles originate from posterolateral margins of the body and are the points at which the arch joins the body. Laminae form a flattened quadrangular structure that slopes downward. Their union gives rise to the spinous process, called spinal process, which extends dorsally and posteriorly from the midline. At the same time, the union between the laminae and pedicles gives rise to transverse processes, which extend dorso-laterally. The processes are sites of attachment for the muscles and sites of articulation for the ribs. In addition to the transverse processes, the articular processes of the vertebrae start at the joints of the pedicles and lamellae. There are two articular process in each vertebra, superior and inferior, and their function is to articulate with the processes of the vertebrae below them [2].

Since the biomechanical model designed herein is aimed at the spinal segments from T9 to L1, the following paragraphs will discuss in detail the anatomical and functional characteristics of the thoracic and lumbar vertebrae, purposely not presenting the other portions of the spine.

1.3.1 Thoracic vertebrae

The twelve thoracic vertebrae (T1-T12) form the median axial skeleton of the rib cage, also performing both the supportive function and protection of internal organs (Figure. 3 [5]) [3].

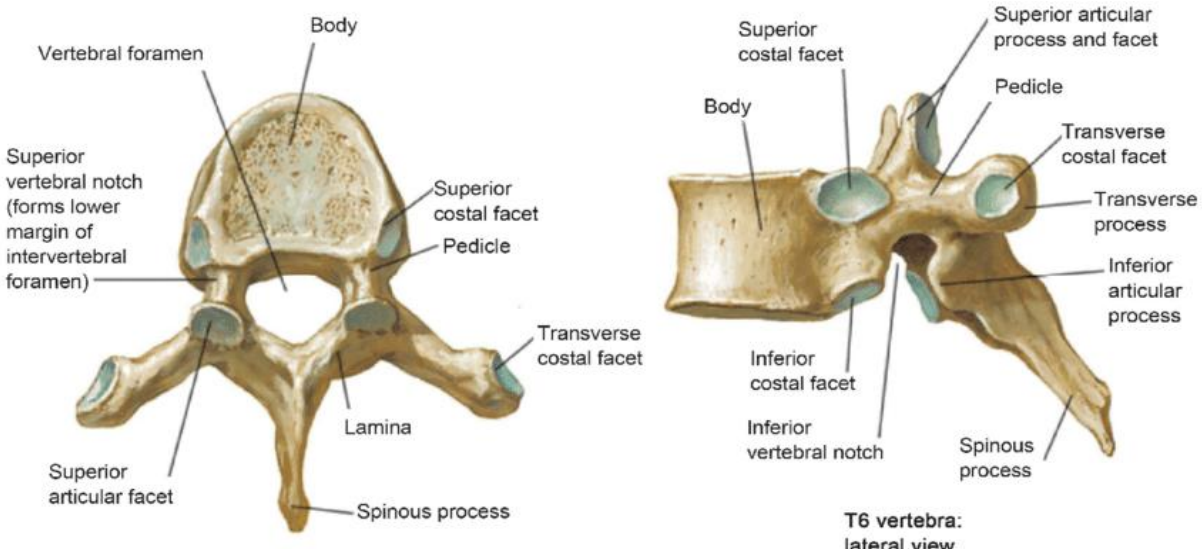

Figure 3: Anatomy of the thoracic vertebrae

According to recent observations [6], the anteroposterior diameter of thoracic vertebra bodies increases progressively from T1 to T12 (to allow for the increase of the load [7]), while the transverse width reduces first in the upper members and then again increases up to T12. Thoracic vertebrae also exhibit rigid vertebral arch and caudally sloping long spinous process. The orientation severely limits dorsal extension movements [8]. Axial rotation is facilitated by the inclination of the thoracic facet joints, with extension and flexion reduced; furthermore, the presence of the thoracic cage to limit the movements of the articular. Extra care needs to be taken for the last two thoracic vertebrae, T11 and T12, which are not fixed to the ribs. T12 is a transitional vertebra between the lumbar and thoracic regions, with both anatomical features of each. As such, T12 limits movements with L1 but allows rotational movements with T11[7].

1.3.2 Lumbar vertebrae

The lumbar vertebrae are the most inferior freely movable segments of the spinal column and consist of 5 vertebrae from L1 to L5 (Figure 4). They vary from the lowest part of the thoracic spine to the beginning of the sacrum, which connects the spine to the pelvis. The major function of the lumbar vertebrae, like the rest, is the protection of the spinal cord during movement but also to withstand mechanical stresses and allow ample flexion and extension [7].

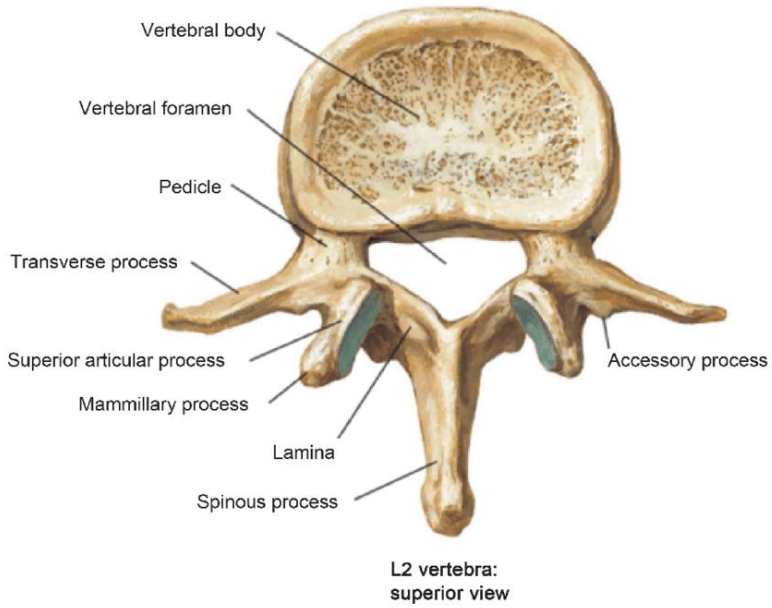

Figure 4: structure of lumbar vertebrae

The superior and inferior articular processes are strongly developed and sagittal oriented, facilitating the extensive flexion and extension movements (Figure 4 [9]).

The greater thickness of these discs is required to resist the greater mechanical stresses of the lumbar spine [2]. Furthermore, the lumbar spine may also be considered as a collection of Functional Spinal Units (FSUs), where each unit comprises two contiguous vertebrae and the intervening intervertebral disc that collectively introduce the required mechanical and motional properties [8].

From a biomechanical standpoint, the lumbar region is characterized by the presence of a physiological curvature, the lumbar lordosis. Such conformation is fundamental since it helps to maintain upright posture and optimizes load distribution along the vertebral column [3]. Clinically, it's not unusual for the lumbar spine to be the site for degenerative pathologies such as herniated discs, spondylolisthesis and spinal stenosis. These pathologies are favoured by the high mechanical stress the lumbar vertebrae experience, particularly in the transition zone: between L4-L5 and L5-S1[8].

In conclusion, the lumbar spine is a very specialized structure designed to combine strength, mobility and safeguarding of the nervous structures in a delicate functional equilibrium that is prone to degenerative processes.

1.4 Intervertebral Disc Structure and Mechanics

The human spinal column is a highly evolved system designed to provide stability as well as flexibility to the body. One of its substantial yet delicate components which allow for this function to be attained is the intervertebral disc (IVD). It is a fibrocartilaginous complex along the entire length of the spinal column, from the first cervical vertebra to the terminal sacral vertebra[10], [11]. In the lumbar region, IVDs are roughly 7 to 10 mm thick and roughly 4 cm in diameter on the anterior–posterior axis. They constitute around 20–30% of the total length of the spine and play a biological function by the delivery of nutrients, and a mechanical one by acting as shock absorbers (Figure 5 [12]). IVDs are the largest avascular structures of the human body since there are no vessels with blood in them, thus, the delivery of nutrients is by diffusion via the pre-discal vessels [7].

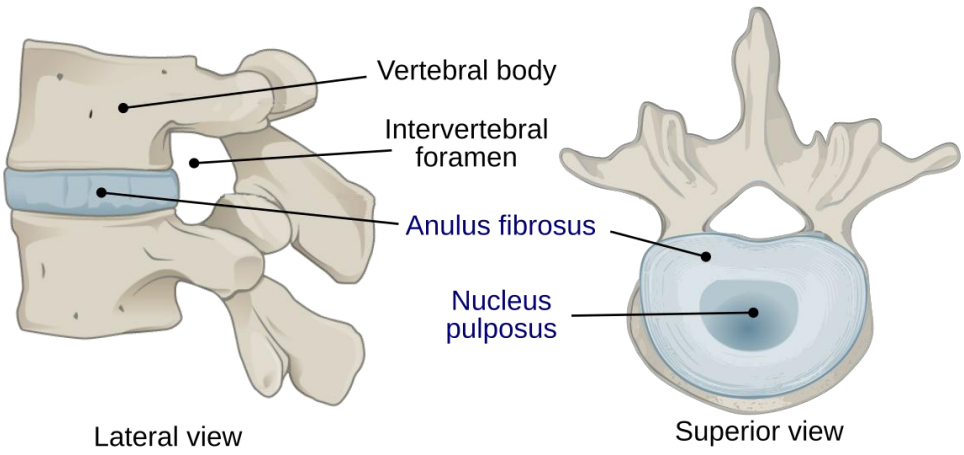

Figure 5: Anatoly of intervertebral discs

Actually, a healthy IVD is an anisotropic structure (i.e., the mechanic properties are function of spatial orientation) capable of shock absorption and allowing movement.[13]

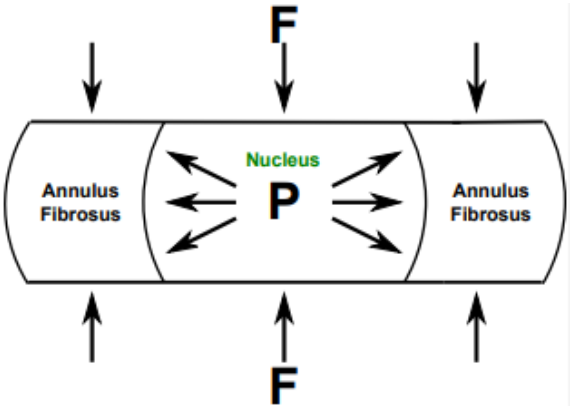

Figure 6.Diagram of the load transfer across an intervertebral disk.

This actuator role is supported by the two structures of the IVD: a tough outer concentric ring of fibrous cartilage called *annulus fibrosus* (AF) that encloses a softer nucleus called *nucleus pulposus* (NP); the NP is capped inferiorly and superiorly by cartilaginous endplates [11].

During daily motions, IVD experiences a large range of deformation, but still has ability to revert to its initial shape (Figure 6 [14]) . Evidently, the load depends upon the position of the disc and upon the movement being considered. When the disc sustains such stresses, the load is transferred to the hydrated nucleus pulposus, which transmits the load in the form of a hydrostatic pressure supported by the AF and endplates [14]. The mechanical function of the disc depends upon its extracellular matrix; indeed, its composition and organization alter the behaviour of the disc. This is a dynamic matrix, consisting of two disparate elements: collagen fibres and proteoglycan content. Collagen confers structure: type I collagen dominates in the outer part of the annulus fibrosus, conferring tensile strength, whilst type II collagen predominates in the inner part and in the nucleus pulposus, conferring resistance to compressive loading. Proteoglycans, particularly aggrecan, are mainly the reason for water retention and in generating osmotic pressure, which is necessary to counteract compressive deformation.[11]

The water content of the disc is critical for maintaining its mechanical and physiological functions. Water provides resistance to compressive loads by generating hydrostatic pressure and allows the AF to distribute stresses evenly during movement. Recent studies have shown that the water content of the disc decreases significantly with age and as disc degeneration progresses. In healthy discs, the nucleus pulposus has a water content of approximately 90% and the annulus fibrosus 65-67%. These high levels of hydration are critical to ensure the disc's ability to withstand daily mechanical stresses and to facilitate dynamic movements of the spine.[15]

1.4.1 Annulus Fibrosus

The annulus fibrosus (AF) is one of the most important components of the human intervertebral disc. Its main function is to create an internal stabilising component capable of containing the NP, maintaining pressure, and preventing compression of the spinal column.[7]

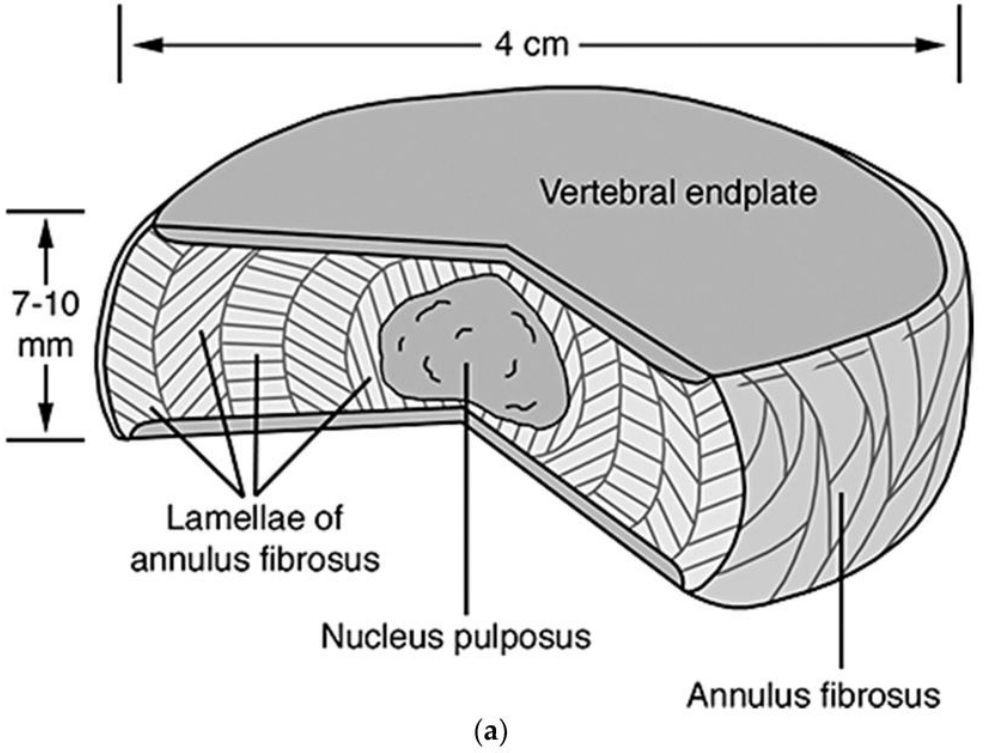

Figure 7: structure of annulus fibrosus

The AF is a fibrocartilaginous tissue formed by 15-25 concentric layers or rings called lamellae to form a multi-layer structure surrounding the NP.[7], [10], [11] . Each layer contains collagen fibres arranged parallel within each lamella (Figure 7 [7]) . These fibres are oriented at approximately 60 degrees relative to the vertical axis (the spinal axis) and at +-25-45 degrees

in the transversal plane, also, the angle of inclination increase towards the centre of the disc and, additionally, the anterior fibres are thicker than the posterior fibres.[10], [11], [13]

Collagen, presents in the annulus, plays an important role as it contributing to the material properties, shape and tissue organization of the annulus itself.[7] In particular, an increased concentration of collagen is observed in the inner zones compared to the outer zones of the annulus. Specifically, there is more type 2 collagen in the inner zones and more type 1 collagen in the outer zones. This distribution is attributed to the properties of type 1 collagen , which provides good anchorage to the bone, and forms a transition zone between soft tissues, such as the nucleus pulposus, and denser, fibrous outer regions of the annulus[16]. The AF are not formed from collagen alone; elastin fibres are also present within it. Located between the laminae, these fibres strengthen the annulus, restoring it to its normal condition after a load has been applied and joining the laminae together[11], [16]. Healthy discs have an annulus with a water content that decreases from the outside to the inside, ranging from 50 to 70 per cent. The collagen laminae and the proteoglycans they contain enable the annulus to resist mechanical loads.[7]

From a biomechanical perspective, the annulus is an anisotropic structure whose properties tend to strengthen and stiffen towards the outside. As in the previous section, the annulus transforms the pressure of the nucleus into a radial force, preventing the disc from protruding [13], [14], [16]. During compression, there is an increase in nucleus pressure and fibre tension. The inner layers are subjected to minimal compressive stress, while the outer layers are also subjected to tensile stress. Due to their orientation, however, they can absorb these stresses. Movement of one vertebra relative to another can cause both shear and strain stresses. The shear stresses can be perpendicular to the direction of the fibres and can cause the fibre itself to break. In addition, the outermost surface structures are more affected by deformation as they are subjected to greater stresses [13].

1.4.2 Nucleus Pulposus (NP)

The nucleus pulposus represents the central and innermost component of the intervertebral disc that moves when changing posture(Figure 8 [17])The disc appears as a gelatinous, avascular and highly hydrated structure located between the two vertebral cartilages and enclosed by the annulus .[7], [10], [18] It is an incompressible structure composed of randomly organized type II collagen fibres, radially interconnected by elastin fibres [11].

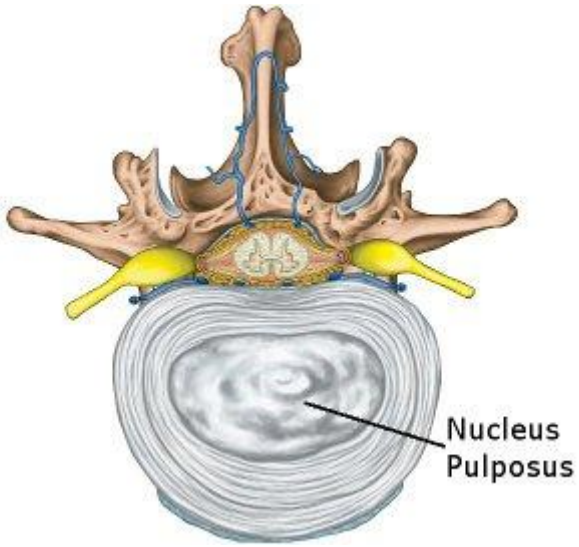

Figure 8: Nucleus pulposus

The NP consists mainly of four elements: type II collagen fibres, elastin fibres, proteoglycans, and water. Each of these components plays a critical role for the performance and health of the NP. Unlike the annulus fibrosus, the collagen fibres form a loose and irregular network connected to the elastin fibres, which enable the disc to return to its original shape and size after mechanical loading.[7] Proteoglycans, in contrast, contribute to water retention within the

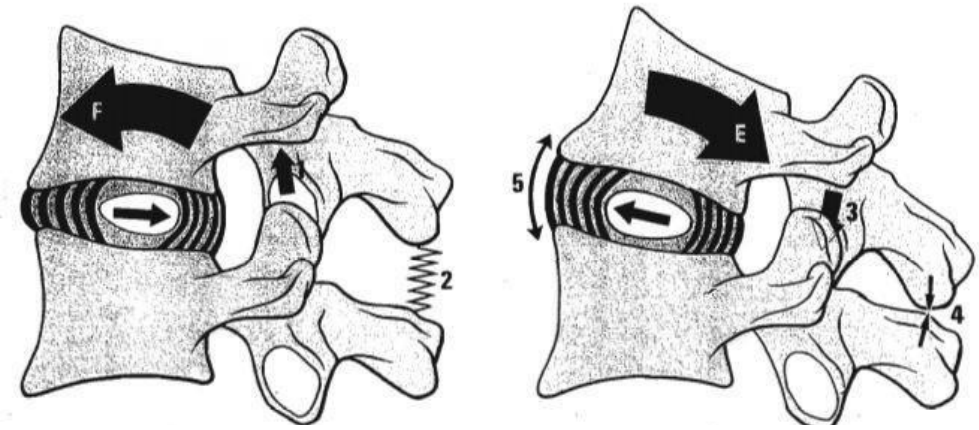

Figure 9: Movement of the nucleus pulposus in the intervertebral discs as a result of flexion

tissue that allows it to resist compression. The nucleus contains a high concentration of water 80-90%, that allows to absorb shock and redistribute it to the vertebrae and annulus.[15]

Biomechanically, the NP behaves as a closed fluid, capable of generating pressure when subjected to axial loads (Figure 8 [19]) . This pressure is then transmitted radially toward the annulus and endplate, that contain it by opposing its expansion. In this way, the function of cushioning and load distribution are guaranteed[13], [16]. Under physiological conditions, the NP is responsible for supporting approximately 70% of the axial compressive force applied to the spine [16].

The ability of the nucleus to generate this pressure is determined by the content of water and proteoglycans, which determine its osmotic potential. Due to these components, an internal pressure of 2.3 MPa is generated under physiological conditions during a load [7]. In the discs, during lumbar extension movements, the nucleus shifts anteriorly, increasing pressure on the posterior annulus fibres. This behaviour confirms the central role this structure plays in balancing forces [8], [18].

1.4.3 Degeneration of intervertebral disc

Intervertebral discs are the first tissues to be damaged because of aging and cause morphological, functional and structural changes. This causes a pathology referred to as disc degeneration [13]. The degeneration of the IVDs is a progressive process that depends on different factors and leads to changes in the geometry, biomechanical behaviour and structure of the disc, affecting its ability to transmit and distribute the load of the spinal column. Today, lumbar disc degeneration is one of the leading causes of low back pain [14], [15]. The main causes for the occurrence of disc degeneration are many including a combination of genetic and

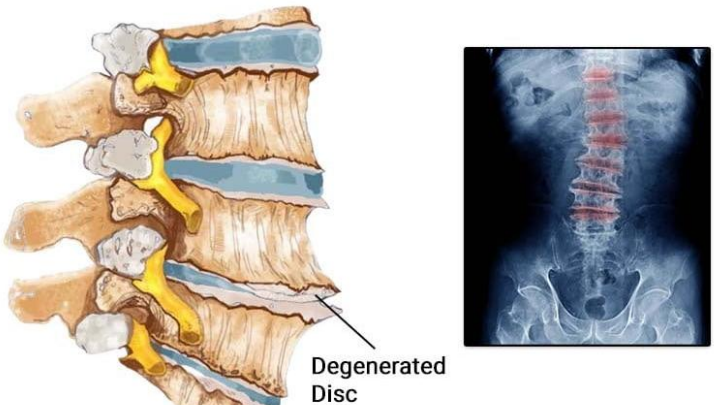

Figure 10:degenerative disc disease

environmental factors such as age, obesity and smoking. The primary causes leading to disc degeneration are believed to be, first, failure of the nutritive relationship with the cells of the disc itself and, second, abnormal biomechanical loads (loads in a certain value range and for a relatively long time of application) [7], [13], [14]. The biomechanical function and reaction of the disc is compromised because the architecture of the extracellular matrix that consists of proteoglycans and collagen fibres is compromised [7].

Therefore, morphologically and structurally, the first alteration that occurs in disc degeneration is the disappearance of proteoglycans(Figure 10 [20]). This change leads to the diminution of nucleus osmotic pressure, and the disc fails to maintain itself properly hydrated in loaded conditions. This causes the AF to resist compression immediately and, as a result, its fibres begin to weaken and harden, which propels the degenerative process [6], [13], [16]. Collagen fibres also alter with degeneration, but not as much as proteoglycans. The amount of collagen is not altered, but the type and distribution may be altered. There is a replacement of type 1 collagen by type 2 collagen, making the tissue more fibrous and less gelatinous [17]. For the clinical setting, T2 weighted sagittal MRI is the most appropriate technique for evaluating disc morphology and degeneration. The most widely used grading for disc degeneration is the pfirrmann classification (Figure 11 [21]). It is based on MRI and evaluates several factors including signal intensity, disc height, disc structure, and distinction between the annulus and the nucleus [18], [19]. The process involves the use of 5 grades:

- Grade 1: The disc has homogeneous structure and hyperintense signal intensity similar to cerebrospinal fluid. The NP is well hydrated and can be clearly differentiated from the annulus fibrosus. Disc height is normal.

- Grade 2: the structure is mildly inhomogeneous, with horizontal bands; the signal remains hyperintense. The nucleus-annulus differentiation is still preserved, and disc height is maintained.

- Grade 3: the disc signal is intermediate, the distinction between nucleus and annulus is increasingly lost, and the disc height may be mildly reduced.

- Grade 4: the disc appears markedly disorganized with hypointense signal and internal distinction completely lost. Disc height is significantly reduced.

- Grade 5: observe very hypointense signal, absence of hydration, completely collapsed structure and gross reduction in disc height [19].

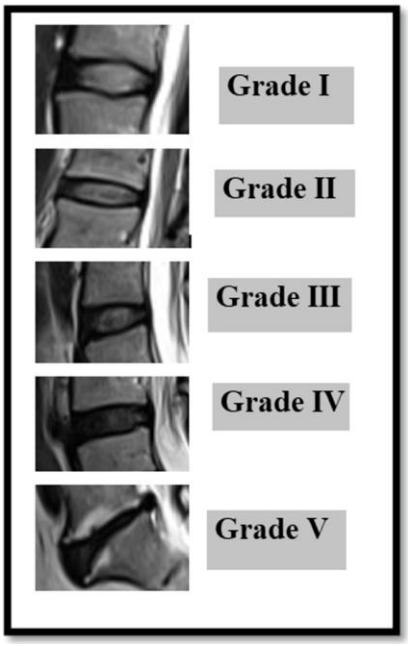

Figure 11:pfirrmann classification

This grading has been found to be very useful in both clinical and research practice since grade can be correlated with other parameters such as signal intensity on MRI, T2 value or lost disc height.[20], [21].

1.5 Finite element Modelling of the spine: State of Art and Biomechanical Applications

Finite element modelling (FEM) is a useful tool in spinal collum biomechanical analysis as it becomes possible to predict the load and the different forces to which the actual vertebrae and discal structure is exposed. its complexity in structure and the interaction between its different component (vertebrae, disc and ligaments) make it difficult to investigate its mechanical behaviour by using the clinical or classical method. FEM analysis surpasses this limitation because it manages to create a physiologic and pathologic model, merge both real geometry of the structure and patient specific characteristics [22],[23].

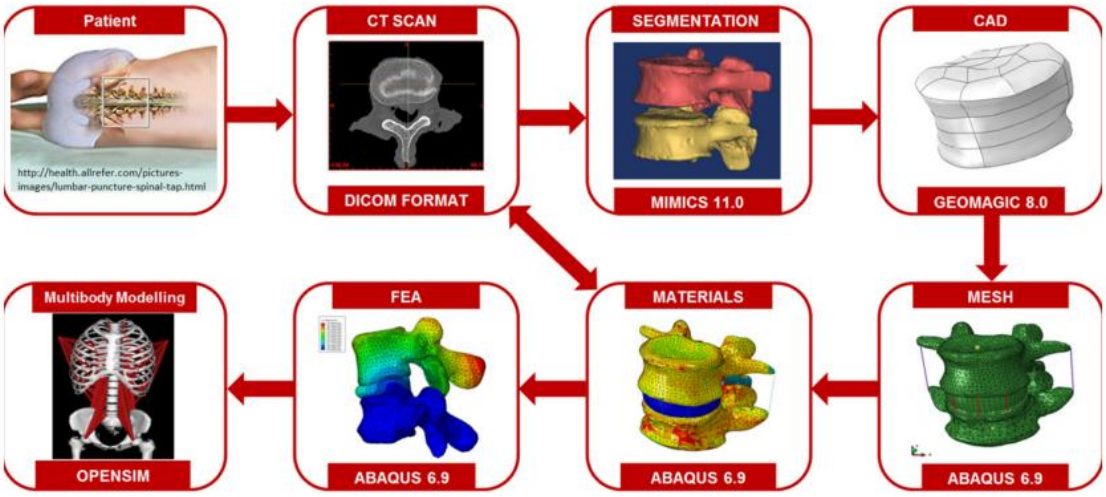

Figure 12:Protocol for creating FE mesh of the functional spinal units

Actually, compared to the clinical standard approach, i.e., dual-energy X-ray absorptiometry (DXA), providing an accurate value of bone density without geometric details, finite element modelling (FEM) has a high predictive capability for mechanical strength of vertebrae because it combines density with real vertebrae architecture in three dimensions [24]. The computed tomography (TC) application is important for deriving a realistic morphology of the bone and to estimate the bone density by way of Hounsfield Units (Figure 12 [25]). This value would be directly projected on to the model mesh to derive spatially variable mechanical properties for validating the prediction of stress and strain distributions [25], [26]. Nevertheless, CT is a useful tool for the bone tissue, but it does not allow to find out the mechanical proprieties of the soft tissue, such as the IVD, since their effective visualization is not possible. Due to this reason, the MRI (Magnetic Resonance Imaging) is essential to get a true representation of the IVD, especially NP and AF. Previous studies have shown that the use of T2-weighted and T2-mapping allows enables characterization of the disc degeneration and identification of the anisotropic characteristics in FEM model [27], [28].

The combination of CT and MRI is suitable since it allows for the creation of a high-fidelity multimodal model, which can properly represent both rigid parts (bones) and deforming parts (ligaments and IVD). Such an approach improves the predictive capability of the model for simulating realistic loads, vertebral fracture risk analysis, evaluating surgical interventions and degeneration mechanical behaviour [29], [30]. The second important factor in

vertebral modelling is the choice of model to be used. The use of an isolated vertebra has been eclipsed by the acceptance of the use of Functional Spinal Units (FSUs), which include at least two adjacent vertebrae and the intervening disc. FSUs allow faithful replication of load transmission, discs and neighbouring vertebrae interaction, ligaments, and posterior joints interaction, as well as biomechanical changes initiated by disease or surgery. More so in the presence of asymmetric or dynamic loading conditions, where the interaction between the different components of the FSU becomes the major force distribution and bone failure mechanism [28], [31], [32].

In the modelling of IVDs is concerned, use of a hyper elastic constitutive equation is optimum to describe the nonlinear mechanical behaviour of the annulus fibrosus. Mooney-Rivlin model was proven suitable for describing the stiffening tissue response under load and anisotropic response. This approach, not considering the fluid component such as in the poroelastic model, is less computationally efficient but also still capable of properly simulating the stress distribution. Finally, tools such as 3D Slicer have also simplified segmentation and constructing anatomical models [33],[34].

Lastly, FEM simulation of the spine, facilitated by CT and MRI, is an end-to-end, patient-specific solution today. The use of free software (FSU), using hyper elastic models such as the Mooney-Rivlin model for discs, and the optimisation of segmentation protocols are the modern pillars for simulating reality.

1.6 Objective and scope of the Thesis

The biomechanical behaviour of the spinal column is a central aspect of biomedical engineering because it allows the understanding of how it responds to different loading conditions. This kind of study has clinical application directly, for instance, in the prevention of spinal injuries, diagnosis of degenerative diseases, and in surgical planning. But the biomechanical models presented in the lectures are based on simplified geometries taken only from computed tomography imaging (CT) and do not reflect the tissue properties provided by imaging. This takes away from the possibility of closely depicting an individual patient's condition, particularly for disc degeneration. The goal of this thesis is to create a three-dimensional, patient-specific model of the thoracolumbar section of the spinal column (T9 to L1) and the adjacent intervertebral disc (IVD), merging CT and MRI images of the same patient.

The main objective of this study is to predict mechanical properties for the IVD based on MRI-derived parameters, to define materials for the model according to the degeneration level.

The task comprises the following steps: semi-automatic segmentation of the vertebrae from CT scans; segmentation of the IVDs from MRI scans, differentiating the nucleus pulposus (NP) and annulus fibrosus (AF) in the less degenerated discs, and representing the more degenerated discs as a single structure; disc grading based on the Pfirrmann grading system; T2 relaxation times measurement using a MATLAB script; construction of calibration curves to estimate the water content, elastic modulus, Poisson's ratio, and Mooney–Rivlin parameters. Lastly, the geometrical discretization of the anatomical structures and the three-dimensional model generation was accomplished using the software HyperMesh.

The thesis is structured as follows: Chapter 1 provides the anatomical and biomechanical review of the spine, vertebra, IVD, with a review of the finite model. Chapter 2 describe image processing, segmentation, alignment and mechanical characterization of tissue. Chapter 3 will be dedicated to FEM application of the developed model and its possible future applications.

Chapter 2.

Materials and Methods

2.1 Acquisition of Clinical Images

The present study has designed a three-dimensional, patient-specific model of the thoracolumbar portion of the spinal column (T9 to L1). These datasets are used to create the model were obtained from a human cadaveric sample, donated by the University of Bologna Department. This lumbar segment was then imaged using both CT and MRI and mechanically tested to see the response of the vertebrae and IVDs to stress. All the images were stored in DICOM format and processed to develop the model.

Computed tomography was used to reconstruct the bony structure of the spine, particularly the vertebrae. Because of its high contrast between bone and soft tissue and sufficient spatial resolution, CT makes it possible to accurately describe the morphology of the vertebral body. Also, voxel intensity values in Hounsfield Units (HU) can be correlated with bone mineral density (BMD), which is useful for future mechanical property assignment based on density. The main parameters of the CT scan are listed in the table 1.

Table 1:CT images acquisition parameters

VOLTAGE	120 kV
SLICE THIKNESS	0.652 mm
mAs	80

Meanwhile, magnetic resonance imaging was used to investigate the soft tissue structures, particularly focusing on the intervertebral discs. MRI allows morphological structure and indirect parameter estimation to be investigated. Two different MRI sequences were used for this. The FIESTA sequence (Fast Imaging Employing Steady-State Acquisition) was used to study the morphology of IVDs, due to its high spatial resolution and high contrast between solid and fluid phases. FIESTA is a steady-state gradient echo sequence that constantly adjusts

excitation and signal acquisition, such that there are always constant amounts of signal. The contrast of the acquired image is responsive to the value of the T2/T1 ratio and thus is useful for imaging structures under hydration. Thanks to its very high spatial resolution and excellent fluid-solid contrast, the Fiesta sequence could be used to distinguish the AF and the NP [35] (Table 2).

Table 2:MRI FIESTA images acquisition parameters

Fild of View (FOV)	220
Slice Thickness	0.69 mm
Number of excitations	1
Echo Time (TE)	108,432ms
Echo Train Length	1

The T2-weighted spin echo sequence was used to estimate the T2 relaxation time of the disc. This is a conventional spin-echo sequence wherein the 90° RF pulse is preceded by a 180° refocused pulse so that one can collect signal decays governed by T2 relaxation. A MATLAB algorithm was used to determine the T2 value from the signal intensity and echo time (TE). From this value, the material properties of the disc could be ascertained [36] (Table 3).

Table 3: MRI Spin Echo images acquisition parameters

Fild of View (FOV)	320
Slice Thickness	0.69 mm
Number of excitations	1
Echo Time (TE)	108,432ms
Echo Train Length	1

2.2 Segmentation of Vertebrae from CT and MRI Images

The segmentation of vertebrae was done using the free open-source software platform *3D Slicer*, used in the medical field for the visualization, processing, and analysis of three-dimensional imaging data. The software offers a broad set of tools for segmentation, registration, and mesh extraction from diagnostic images, making it particularly well-suited for biomechanical studies based on patient-specific models. Segmentation refers to the process of identifying and isolating specific anatomical structures from medical images, by assigning labels to different regions of interest within the volume. In this case, the goal was to extract the vertebral bodies from CT scans. The CT images were imported in DICOM format into the segmentation software 3D Slicer (Figure 13).

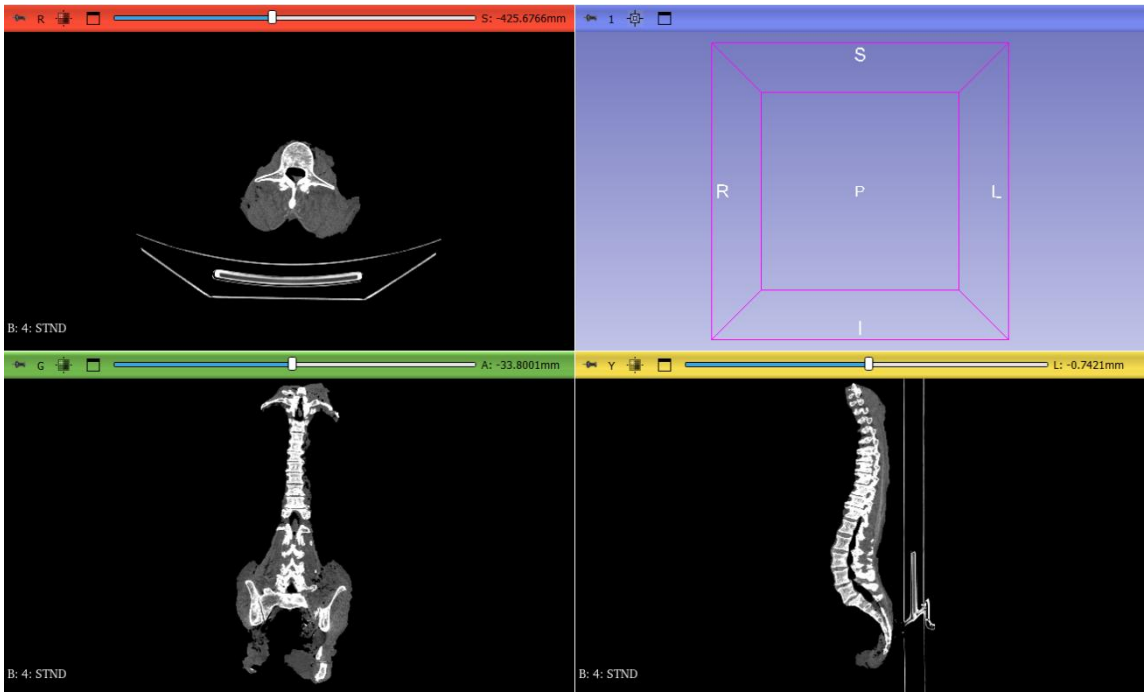

Figure 13: Importing CT images into the 3D Slicer environment

The contouring could happen both in automatic and manual ways. In particular, the edges of the bone components are automatically identified by grey tone interpolation curves of the voxels. This semi-automatic segmentation was used in order to set a threshold to isolate the high-density regions corresponding to bone, by using the Hounsfield Unit values. The segmentation can be carried out either automatically or manually. In particular, the external edges of the bony structures are automatically identified using interpolation of grayscale voxel

intensities Semi-automatic segmentation was used, where a best threshold value was determined for discriminating the high-density regions corresponding to bone by exploiting the Hounsfield Unit (HU) values (Table 4)

Table 4: Threshold values for vertebra segmentation.

Threshold Range (HU)	
Min value	Max value
78.18	1726.42

Once a threshold range appropriate was established, the outer limits of the vertebrae were segmented automatically. This was manually edited slice by slice to further improve segmentation accuracy, until the fine representation of the original volume was reached. Each vertebra between T9 and L1 was isolated as an independent structure within the software, where anatomical labelling and individual STL export for further processing could be performed. The segmentation quality was evaluated by visual inspection on the axial, sagittal, and coronal planes with anatomical coherence and the elimination of topological faults. The precision of this stage was seen as being of utmost importance for multimodal registration accuracy (Figure 14).

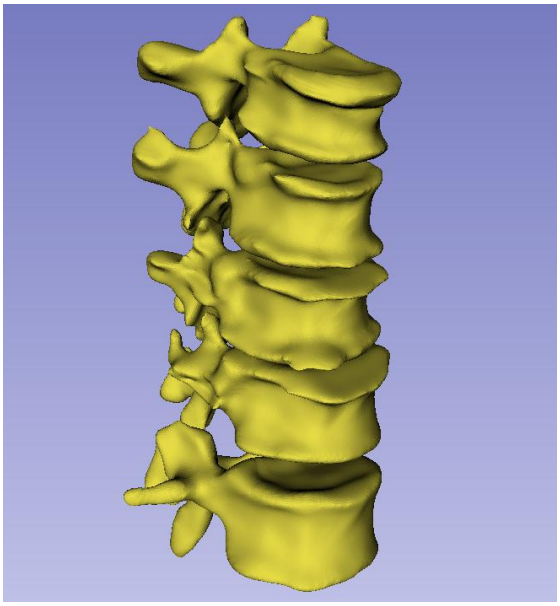

Figure 14: final vertebrae segmentation from CT images

The same procedure was applied to the MRI images, segmenting the vertebrae once again. Although this step was not required for the construction of the final model, it was essential for performing the alignment between the CT-based model and the MRI scans. In this case, the segmentation was carried out using the Local Threshold tool available within the Segment Editor module of 3D Slicer. This tool allowed for more precise control of voxel selection based on localized intensity statistics, which was necessary due to the different contrast characteristics of MRI data compared to CT.

Appropriate threshold values (Table 5) — distinct from those used for the CT images — were defined through testing and visual inspection to best capture the vertebral structures in the MRI scans.

Table 5:Threshold values for vertebra segmentation in MRI images

Threshold Range	
Min value	Max value
2493.59	14468.30

Once the threshold was set, the segmentation proceeded in the same manner as previously described: automatic contour extraction followed by manual refinement, slice by slice, to ensure anatomical accuracy (Figure 15).

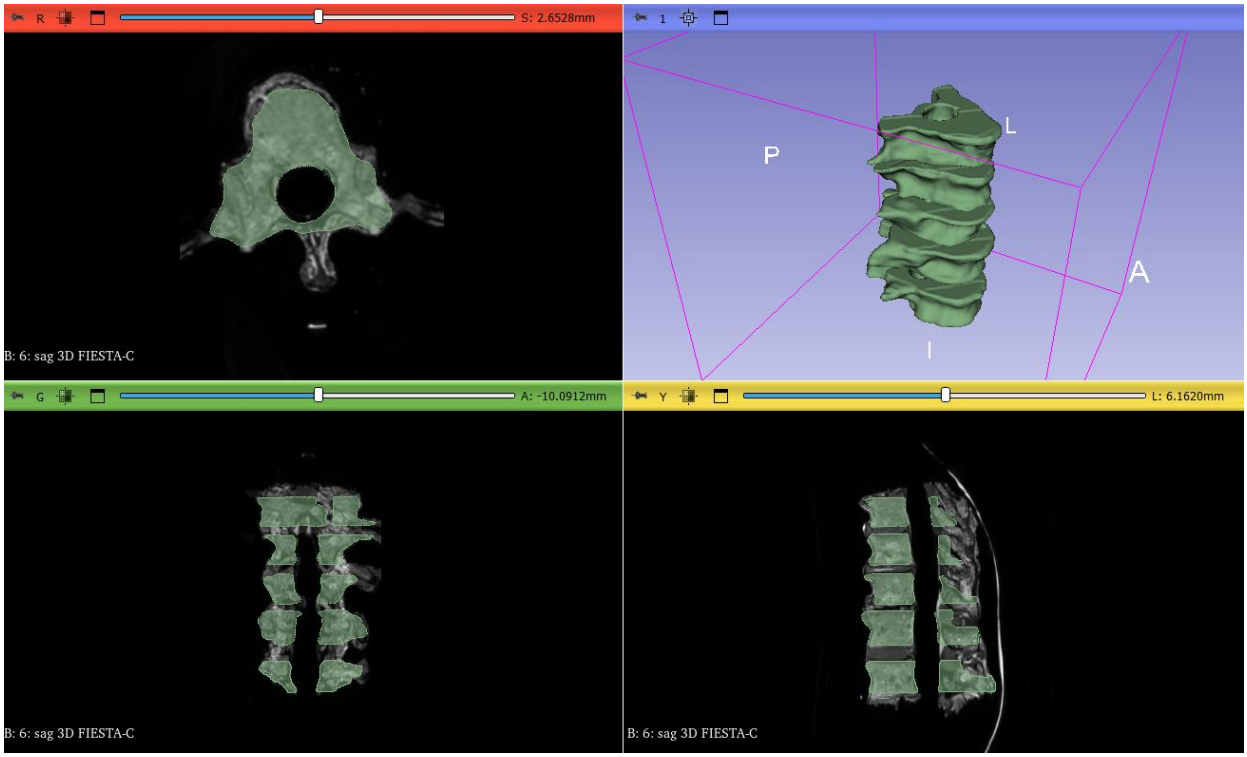

Figure 15 : final vertebrae segmentation from MRI images

2.3 CT-to-MRI Alignment: Alignment of CT Segmentations to the MRI Coordinate System

For purposes of enabling direct comparison between anatomical structures outlined from MRI and CT - as well as accurate transfer information between the two imaging modalities-, it is essential that both models be formulated within the same so axial reference system. CT and MRI images are usually obtained independently, often a different time, under different acquisition protocols and patient positioning arrangements. Therefore, the respective 3D segmentation, even if they are derived from the same anatomical structure, tend to be misplaced both in position and orientation in space. These misaligned pose a primary challenge, particularly in the context of this thesis, where the goal is to produce a 3D anatomic model o the spine which combines the high geometry accuracy if CT-based segmentations and the functional and tissue-level information of IVD from MRI-based segmentation (Figure 16).

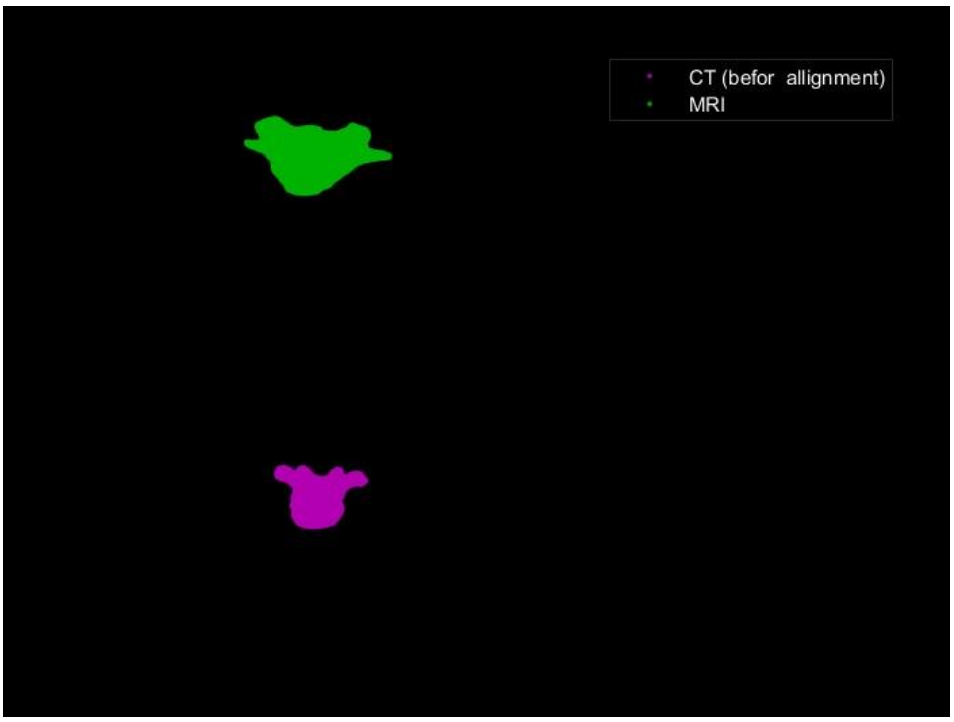

Figure 16: Initial Spatial Misalignment Between CT and MRI Segmentations of Vertebra T9

To achieve this integration, it is necessary to project the CT model of vertebrae into the spatial reference system of the MRI data. For this, a script was written in MATLAB environment that

use the *Iteractive Closest Point* (ICP) function, which is most often used in 3D surface registration. This script aims to make a rigid transformation of the vertebrae's CT model, with translation and rotation only but no deformations, so that they overlap as closely as possible on the model segmented by the MRI. The MATLAB script begins with the loading of two segmented 3D models both saved in STL format: a first vertebral segmentation by MRI and a second vertebral segmentation by CT. Both models are initially saved as triangulated surfaces, composed of an array of points in space and their connectivity. To go ahead and process them with the ICP algorithm, the surfaces are converted to point clouds through the *PointCloud* function, which creates a simple but effective geometric structure where each point is a point of the segmentation of the vertebrae. The *pcregistericp* function is now used at this stage. This algorithm iteratively identified correspondences between the point of moving cloud (segmentation of vertebrae from CT scans) and that in the fixed cloud segmentation of vertebrae from MRI). In every iteration, the rigid transformation tries to minimize the average distance between the pairs of matching points. Iterations are terminated when the distance between two successive transformations is zero or less than a predetermined convergence tolerance. The final product of this algorithm is a rigid transformation matrix and a new transformed point cloud whose coordinates are now in the spatial coordinate system of the MRI (Figure 17).

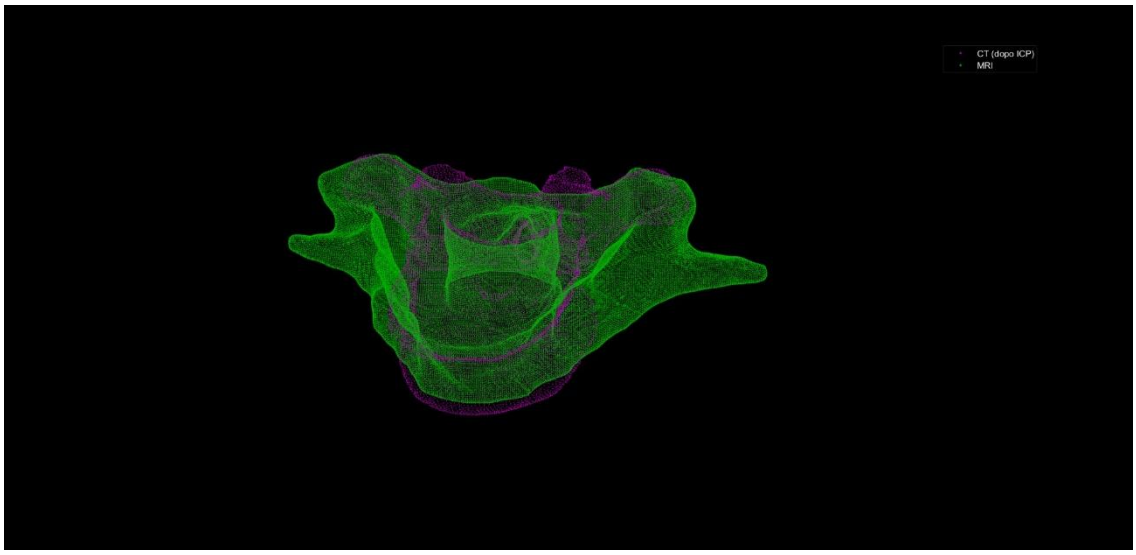

Figure 17: Final Alignment of CT Segmentation to MRI Reference Space for Vertebra T9

To obtain a new STL model, the transformed coordinates are combined with the original connectivity of the CT files through the triangular function. This process allows to maintain the triangular structure of the bone model and its geometric precision. The model is subsequently exported as an STL file through the *stlwrite* function. This was executed for all vertebrae segmentations, from T9 to L1. Only thanks to this align that the morphological data obtained from CT and MRI can be properly superimposed in a way that will produce an integrated model having the high anatomical accuracy of CT scans but, at the same time, the physiological and pathological state of the IVD as provided by MRI images. The 3D model obtained can therefore be not only anatomically correct but also biologically informative.

2.4 MRI-Based Segmentation of Intervertebral Discs

The anatomic trait, that was used to create the model of the intervertebral disc, included all the IVDs from T9 to L1 vertebrae (T9–T10, T10–T11, T11–T12, T12–L1). The segmentation of the IVDs was done on the software 3D Slicer from MRI scans (Figure 13.). The goal of this step was to appropriately identify the morphology of each disc and, where possible, to separate the annulus fibrosus from the NP in order to have a morphologically uniform representation of disc anatomy (Figure 18).

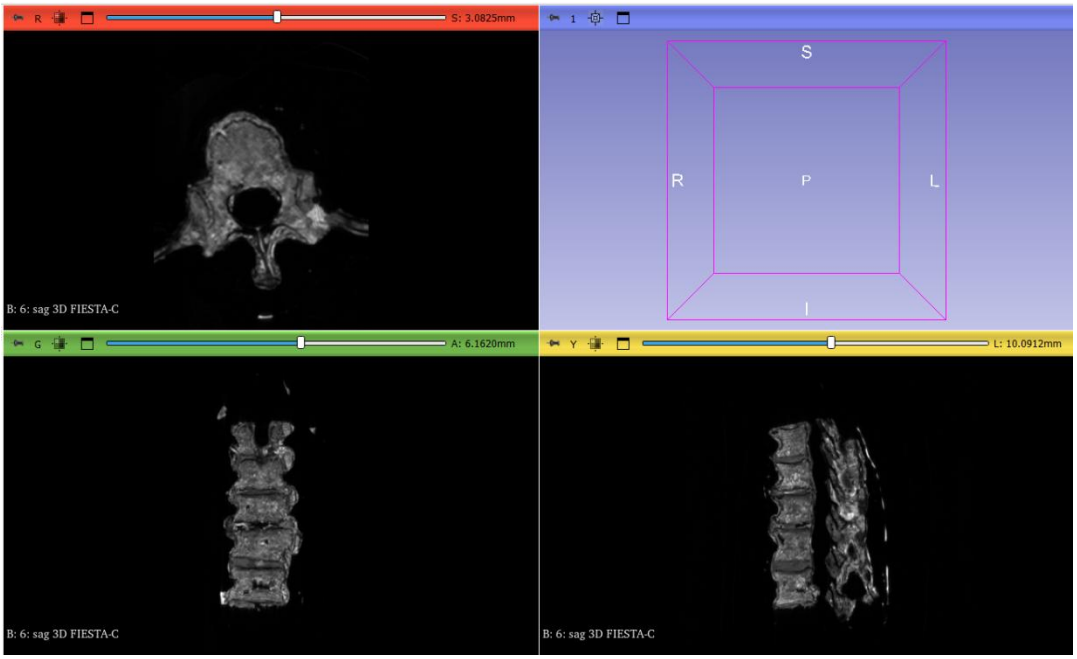

Figure 18:Importing MRI images into the 3D Slicer environment

Initially, each disc was segmented as a single structure, without a division between annulus and nucleus. This segmentation was performed entirely manually. For each disc, a combined approach was used taking the coronal, sagittal, and axial views into account to precisely identify the edges of the disc. In particular, the sagittal view was used to complete the 3D contour of the disc in order to describe it uniformly throughout its thickness. Even though delimitation was carried out with utmost caution, disc size overestimation was allowed in order to capture the entire anatomical structure and avoid underestimation of disc volume. Smoothing was applied afterwards to regularize the entire disc surface (Figure 19).

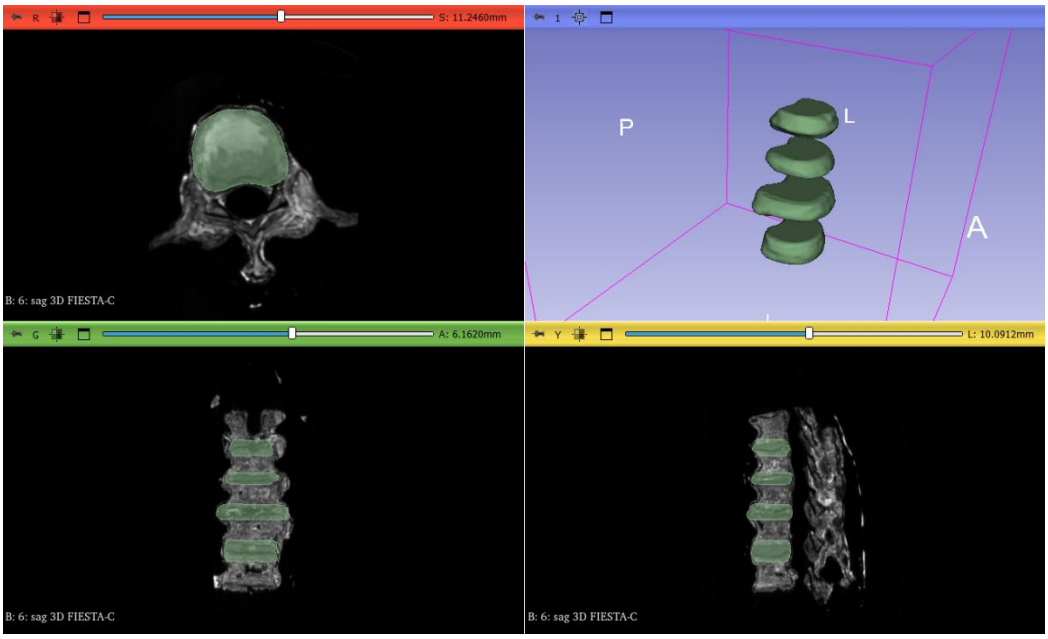

Figure 19: disc segmentation from MRI scans

Once the disc segmentations were completed, the next step involved the segmentation of the NP, which was performed only where this structure could be clearly identified. It was possible for T9–T10 and T12–L1 discs alone. In these discs, the MRI images showed a central hyperintense region, which corresponds to high water content. This brightness is related to the high-water content of the nucleus, which in healthy discs can reach 80–90%. The tissue's hydration is an attribute that directly impacts the T2 relaxation time, a parameter that control signal intensity of MRI images. Particularly for hydrated tissues, T2 relaxation time is longer, providing a brighter intensity of the signal: the higher the water content, the greater the T2 relaxation, and the brighter of the tissue. The segmentation of the nucleus was also performed

manually, again using the three orthogonal planes and signal intensity criterion (Figure 20). A final smoothing step was used to ensure surface regularity [37], [38] [39].

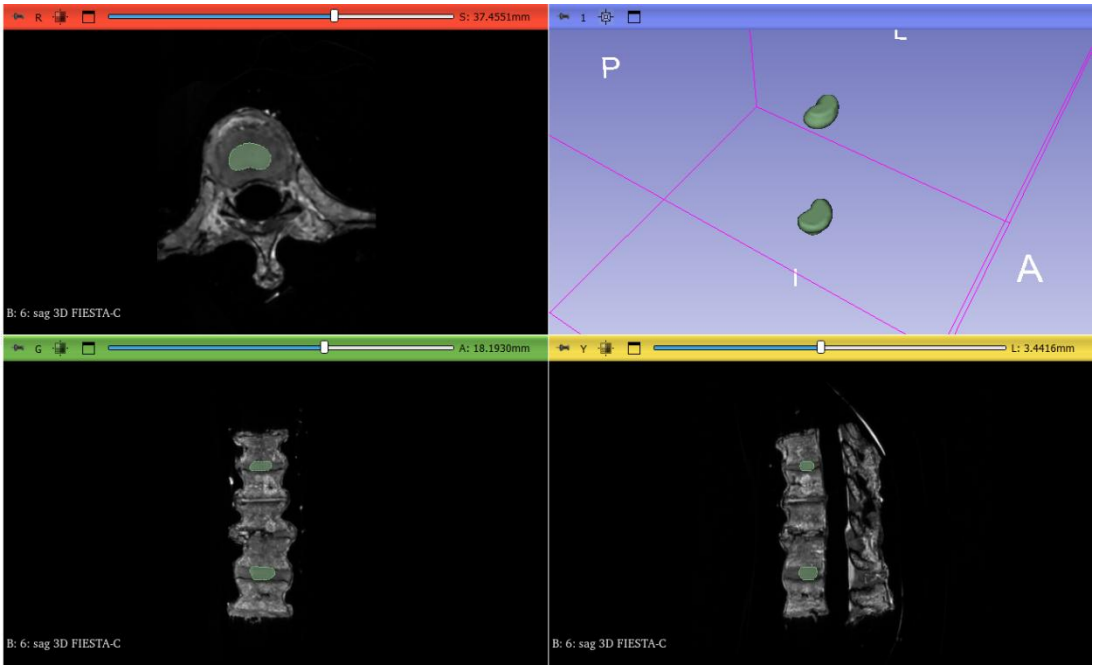

Figure 20: nucleus segmentation from MRI images

In the T10–T11 and T11–T12 discs, segmentation of the nucleus was not possible, as MRI images showed a homogeneous signal intensity. This is related to an advanced stage of degeneration, in which water loss and matrix breakdown eliminate the visual distinction between NP and AF. In these cases, the discs were considered solid undivided structures.

Once the segmentation of the discs and, where possible, the NP had been obtained, the next fundamental step in the final model determination was carried out: the application of logical operations. Through these operations, any overlap or geometric interference between adjacent structures can be controlled exactly, improving the overall quality of the segmented model. In the 3D Slicer program, they are provided with the Logical Operations Tool, part of the Segmented Editor module. In the present study, the logical operations were carried out in two major steps. The initial step was aimed at eliminating any intersection of the intervertebral disc (IVD) with the adjacent vertebral bodies. In this case, the segmentation of the vertebrae was kept fixed and the portion of the disc overlapping with the vertebral volume was eliminated.

This facilitated simple separation between the two structures so that non-physiological intersections are avoided, and geometric consistency of the model (Figure 21- Figure 22).

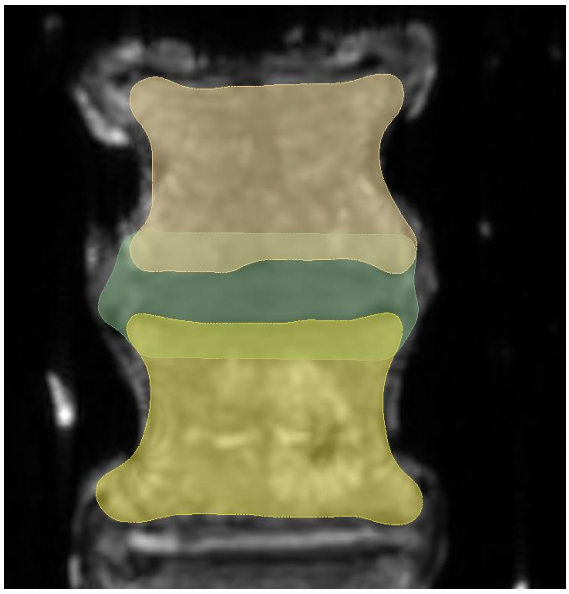

Figure 21:Initial segmentation with overlap between intervertebral disc and adjacent vertebrae

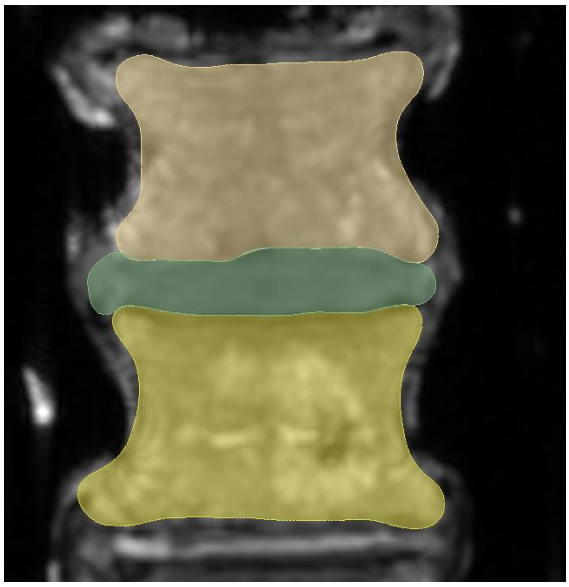

Figure 22: Result after Boolean subtraction between disc and vertebrae

The second logical operation was performed for the two discs in which there is obvious separation of the NP and AF. Here, the intention was to define clearly the geometry of the annulus fibrosus by separating the volume of the whole disc from the volume of the nucleus and hence obtaining the remaining outer region. This operation further enhanced discrimination between disc components and contributed to more accurate and detailed description of the segmented structures. Overall, these operations were vital towards establishing an anatomically consistent and topologically clean 3D model. Particular attention was taken to maintain surface continuity between segmented surfaces, and to avoid gaps or overlaps, as a method of offering a robust and reliable platform for further modelling, analysis, or simulation steps (Figure 23).

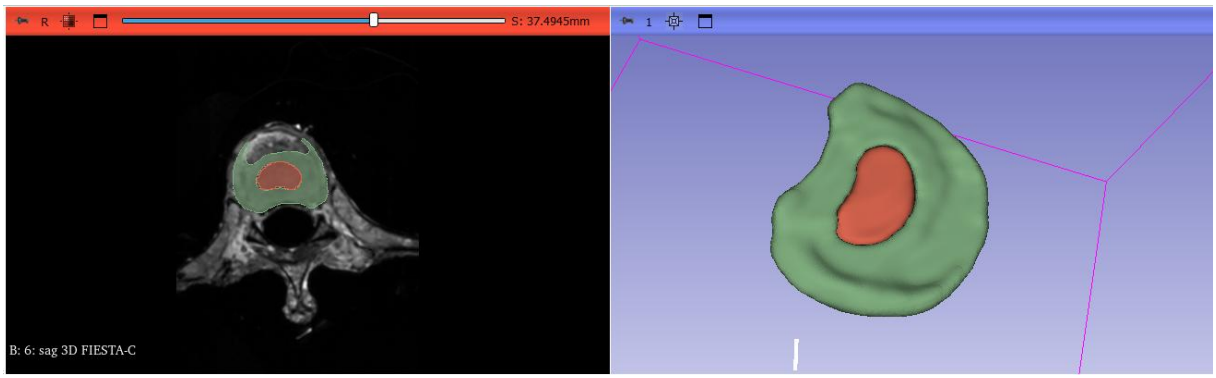

Figure 23: final 3D anatomical model of the intervertebral disc: annulus fibrosus and nucleus pulposus

2.5 Estimation of T2 Relaxation Time Using Simulated Annealing

After the segmentation of intervertebral disc from MRI images was done through 3D slicer, the next aim was to estimate, for discs, nucleus and annulus , the relaxation time T2, a value which is proportional to the water content of the tissue. This value is important in the application of individualized mechanical properties to the disc for Finite Element Model (FEM). With best conditions, the T2 value could be obtained by using multi-echo sequences, which allow fitting the whole exponential decay curve of the signal. The dataset contains one spin-echo sequence with one echo time value (TE = 108,432ms), so direct fitting is impossible. To bypass this limitation, it was established to estimate T2 time using a numerical optimization algorithm. However, for the algorithm to be able to provide a good approximation, it needed to be given an appropriate starting range from which it could start. In this case, the range is a reasonable T2 range that is to be different than healthy and degenerative discs. This is an important aspect in the case of the chosen algorithm, that is the simulated annealing, is a probabilistic method founded on the physical annealing process employed in metallurgy. During the optimization process, the algorithm explores the solution space by increasingly accepting worse solutions to have a non-zero probability to escape from the local minima and then progressively decrease this tolerance to converge to an optimal solution. Because of this ability to escape local minimum, simulated annealing is superior to traditional deterministic algorithms. For this study, the *simulannealbnd* function of MATLAB was used, which applies the algorithm with provided lower and upper bounds on parameter estimates. Hence, it was necessary to classify each disc, so that it could be decided whether it was healthy or degenerative and for finding the correct initial bounds for T2 estimation.

The standard Pfirrmann classification, which compares the T2 signal intensity of MRI images, was not possible to apply here since only the TE value is provided. Therefore, we apply an alternative Pfirrmann classification using a geometric parameter: the height of the discs. This approach procedure is also supported by the literature [40], [41] that report a correlation between degeneration and disc height. The height of every disc was subsequently measured in 3D slicer using the third procedure described and used by Guellil et al. (2022) [42], which involves calculating the mean between anterior, central and posterior disc heights in sagittal view (Figure 24).

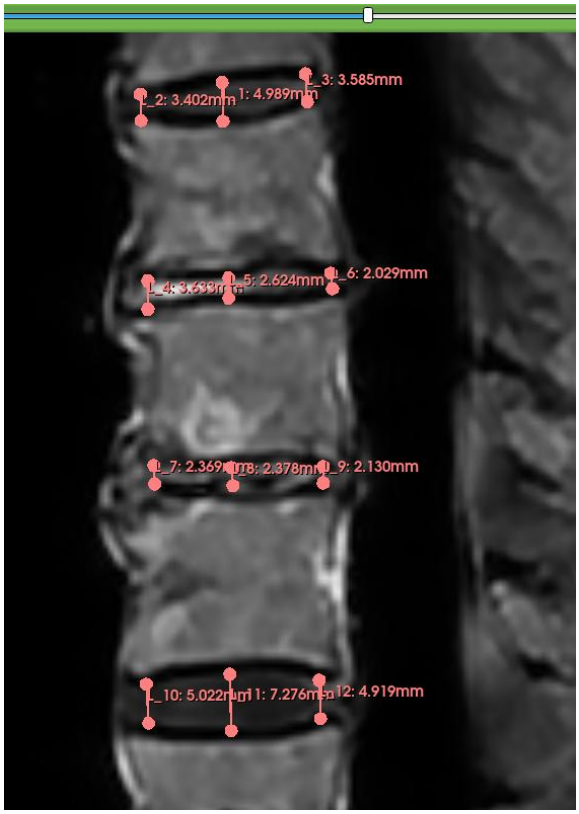

Figure 24: Measurement of Intervertebral Disc Height on Sagittal MRI: Anterior-Central-Posterior Averaging Method

These values were compared to a control value height of each IVD, derived from Frost et.al. (2019) research [7]. On this basis, percentual height reduction threshold was determined, based Cetin et al. (2023) and Chen et.la (2023) [40], [41]. In this way each interval was associated with the degenerative Pfirrmnn grade but reinterpreted structurally (Table 6-Table7).

Table 6:Height-Based Pfirrmann Classification

Pfirrmnn grade	*Height*	*Description*
I	100%-85%	Healthy, hydrated disc.
II	85%-70%	Mild height reduction, initial dehydration.
III	70-60%	Moderate height reduction, initial structural changes.
IV	60%-50%	Significant height reduction, evident degeneration.
V	<50%	Disc collapse, severe dehydration.

Table 7:Pfirrmann classification of all IVD

IVD	Height value	Normal height (Frost e.la. 2019)	Reduction	Pfirrmann Grade
T9/T10	4.989 mm	4.90mm	No reduction	I
T10/T11	2.761mm	6.50mm	Significant reduction(40%)	V
T11/T12	2.939mm	5.40mm	Advanced reduction (50%)	IV
T12/L1	5.730mm	6.80mm	Mild reduction	II

Optimization algorithm - simulated annealing - requires initial values to operate. Particularly, T2 value was set to vary from 80 to 120 ms for healthy disc, and from 30 to 70 ms for degenerated discs [43]. Once the range was established, the T2 estimation process could be initiated. For each disc (and each nucleus) the mean signal intensity SI(Te) was retrieved by 3D Slicer from the Segment statistics tool (Table 8).

Table 8:Signal intensity values

Structures	*Signal Intensity*
Nucleus T9/T10	378.944
Annulus T9/T10	300
IVD T9/T10	300.751
IVD T10/T11	490
IVD T11/T12	578
IVD T12/L1	325
Nucleus T12/L1	286.825
Annulus T12/L1	412

This value was used to pull out the T2 using a MATLAB script with a predetermined exponential decay function:

$$SI = SI_0 e^{-\frac{Te}{T2}}$$

Since the system was underdetermined (two unknowns and one equation), a randomized optimization method was used. The simulated annealing method, utilized by using MATLAB's *simulannealbnd* function, explores the solution space with diminishing probability of getting

stuck in local minima. The script optimized the objective function of the squared error between the measured and estimated signal:

$$Error = (SI(TE) - SI_0 e^{-\frac{Te}{T2}})^2$$

For both disc and nucleus pulposus, 50 independent optimizations were performed, beginning from a random starting point within the specified intervals for T2 and for SIo. This was to avoid the effect of the choice of the starting point on the outcome, which can greatly influence the outcome in stochastic algorithm. By generating 50 different initial points, the intention was to reduce any initialization bias induced and ensure the final solution was a result of a broader exploration of the space solutions. For each 50 optimizations, the simulated annealing algorithm estimated a pair of parameters (T2 and SIo). The mean and the standard deviation of T2 values were calculated at the end of this process.

Values estimated confirmed the methodology: disc of a healthy exhibited more than 100 ms mean T2 values, while degenerated discs exhibited values. This method allowed it to provide a well-reproducible and physiologically quantitative estimation of water content even under inferior imaging conditions.

2.6 Biomechanical Characterization of the Nucleus Pulposus

The NP is the central component of the IVD and perform a primary essential function in the spinal biomechanical, i.e., controlling compressive load. It is a heavily hydrated tissue, compressed by water and proteoglycans, and confers on it hydrostatic and viscoelastic properties. Its heavy fluid content allows the nucleus to dissipate the axial loads effectively and assist in disc structural stability [44], [45]. In order to correctly represent the nucleus 's behaviour in the numerical model, it must be given the mechanical properties which reflects its actual composition. Specifically, the elastic modulus and the Poisson's rate are strongly dependent on its water content. More water content, normally, corresponds to more deformability and fluid-like response, whereas lower hydration is related to more stiffness [46], [47].

In this study, predefined or constant values for these mechanical parameters were avoid. Instead, a subject-specific approach was adopted, based on the quantitative water content estimation from T2 relaxation values derived using MRI, described in the last paragraph. This methodological assumption is supported by several studies in the literature where a relationship between T2 and water content is explored. For example, Weidembaum et al. (1992) [48] highlight a reverse relationship between 1/T2 and water content in the IVD, while Marinell et la. (2010) [49] and Nazari et la. (2015) [47] confirm that the T2 values can be a marker of the hydration of the tissue. At the end, Yang et la. (2020) [46] demonstrated the value of this estimation with galvanometric data. Therefore, the use of the T2 values to determine the water content and mechanical properties thereafter is a viable method for physiologic characterization and non-invasive evaluation of the nucleus.

The water content is then calculated to get both the elastic modulus and Poisson's rate based on independent calibration curve from known relation. All the properties were derived by employing a particular method, each of them from a physiological relation between the tissue's behaviour and its mechanical response. This characterization was directly applied to the T9/T10 and T12/L1 IVD, where the nucleus could be segmented independently. Disc with high grade of degeneration, such as T10/T11 and T11/T12, are not included to this analysis, because of their behaviour was more like the AF.

The following section describes the key steps that led to water content estimation and the subject-specific assignment of the mechanical properties of the nucleus pulposus, with realistic and physiologically basis for its integration in the numerical model.

2.6.1 T2-Based Estimation of Nucleus Pulposus Water Content

The relaxation time T2, calculated from MRI information, is sensitive to the biochemical composition of soft tissues, and particularly to their water composition. It is generally assumed that tissues with high hydration have larger T2 values, whereas reduced hydration results in a reduction of the relaxation times. This is in accordance with the dynamics of the interaction between water molecules and the extracellular matrix framework [49], [50], [51]. Several studies have established the existence of a linear relationship between T2 values and tissue water content. Marinelli et al. (2009) correlated the human and bovine intervertebral disc samples and found a direct correlation between MRI-measured T2 values and the gravimetrically measured percentage of water. Correspondingly, Chiu et al. (2001), in a vitro experiment on human discs, also found a similar behaviour, with T2 values diminishing corresponding to water content reduction. Weidenbaum et al. (1992) further established this trend, indicating that T2 is largely affected by water content concentration, with its relationship to proteoglycan concentration being less indicative. Other studies, such as those of Chatani et al. (1993) and Crooks et al. (1987), confirm this linearity.

Based on these findings, in the present study water content of IVD (particularly of the NP) was estimated by employing mean T2 values from MRI. Since Marinelli et al. (2009) and Weidenbaum et al. (1992) original data were not tabulated but only provided graphically, the values were extrapolated manually with the assistance of *PlotDigitizer*. This program is open source and allows for a user to extrapolate numerical data from plots of scientific data in raster image format. The user imports the plot and subsequently calibrates the Cartesian axes by specifying known numerical positions on at least two points along each axis. This allows the software to translate pixel location into real coordinates. The user is then able to click directly on the plotted data points, and the program returns the corresponding (x,y) values.

In this study, water content (%) and T2 (ms) pairs were the data obtained. The data were then digitized and processed using MATLAB and then a linear regression was performed to construct the calibration curves. The following was employed to model the correlation:

$$T2 = a * (\%W.C) + b \quad \Longrightarrow \quad \%W.C = \frac{T2}{a} - b$$

Two independent calibration curves were made and used. The first was made exclusively from the data given by Marinelli et al. (2009), which demonstrated a clear correlation between T2 and nucleus water content. The second has been produced by the combination of the nucleus data of Marinelli (2009) and Weidenbaum (1992). This approach allowed a broader calibration curve that could fit the variation observed over a larger range of hydration states.

After linear fitting, the following final calibration equations were utilized during this work:

- Marinelli 2009 combined with Weidenbaum 1992 (Figure 25):

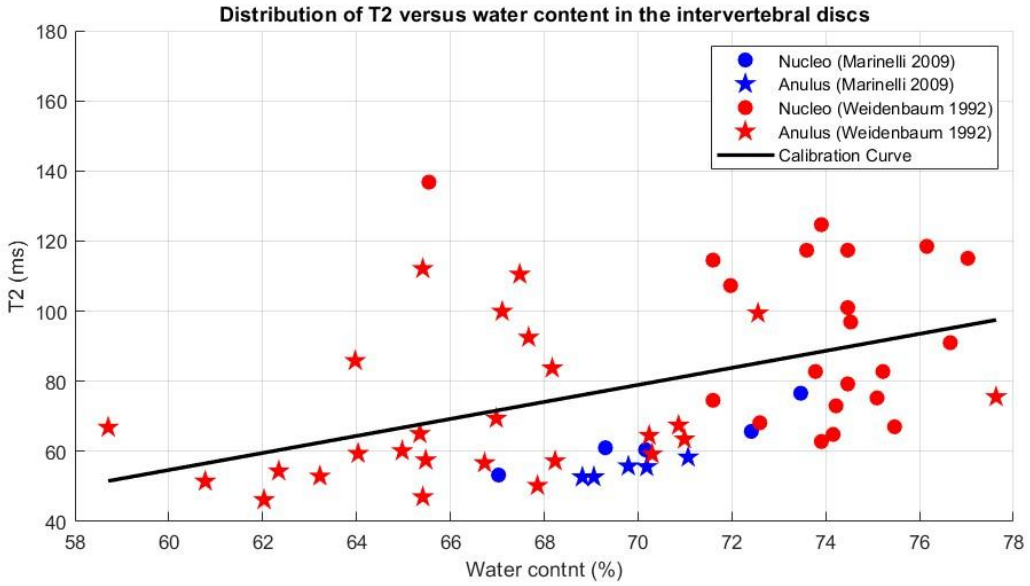

Figure 25:Distribution of T2 versus water content in the intervertebral discs

$$\%W.C = \frac{T2 + 82.69}{2.258}$$

- Only Marinelli 2009 (Figure 26):

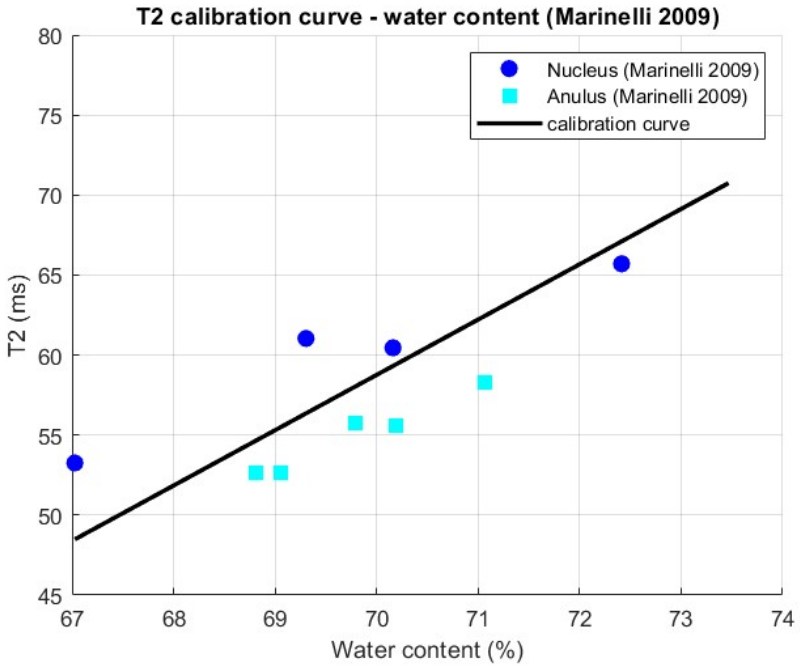

Figure 26: T2 calibration curve - water content

$$\%W.C = \frac{T2 + 183.2}{3.475}$$

In this way it was possible to relate the estimated T2 values and the corresponding percentages of water content for all the structures under investigation. But only the values related to the nucleus pulposus will be used for the mechanical characterization in the model. Two calibration models were employed to estimate water content from the T2 values obtained from the MRI images: one from the Marinelli et al. (2009) data only, and the other obtained by combining the Marinelli (2009) and Weidenbaum et al. (1992) data.

Finally, the curves were used to determine the water content of the nucleus pulposus based on the T2 values obtained from the MRI images, thus making it possible to use a non-invasive quantitative description of tissue hydration status in the following phases of the biomechanical analysis.

2.6.2 Estimation of the Elastic Modulus of the Nucleus Pulposus

Intervertebral disc degeneration is characterized by a gradual reduction in water content of the nucleus pulposus (NP) due to proteoglycan depletion and a change in the extracellular matrix. The reduction in water changes the mechanical behaviour of the nucleus, which becomes increasingly stiff and less deformable under load [52],[53].

To estimate the elastic modulus of the NP as a function of its water content—previously calculated from the T2–%water content calibration curve—an empirical calibration curve was drawn based on experimental data from literature. Specifically, experimental values by Natarajan et al. 2006, Lin Xin Guo et al. 2016 and Qasim et al. 2014 were utilized. These experiments correlate values of elastic modulus with various water content levels in the NP, ranging from about 1 MPa (85% water) to 1.66 MPa (76% water) [50], [54], [55] (Table 9).

Table 9:Elastic modulus from Literature

Elastic modulus	*%W.C.*	*Reference*
1 MPa	85%	Natarajan et al. 2006 [50]
1.5 MPa	80%	Lin Xin Guo et al. 2016[55]
1.66MPa	76%	Natarajan et al. 2006[50]
1MPa	85%	Qasim et al. 2014 [54]
1.2MPa	80%	Qasim et al. 2014 [54]
1.2MPa	78%	Qasim et al. 2014 [54]

The qualitative relationship between the water content of the nucleus pulposus and its mechanical rigidity is well documented in the literature, but no explicit description of the functional form of this dependence has been found. Qualitative dependence of the mechanical stiffness of the nucleus pulposus on its water content is well established in the literature, yet no functional form of this dependence was explicitly stated. Due to this, every form of fitting (linear, logarithmic, exponential) was tried on the given experimental data to choose the best-fit mathematical model (Figure 27).

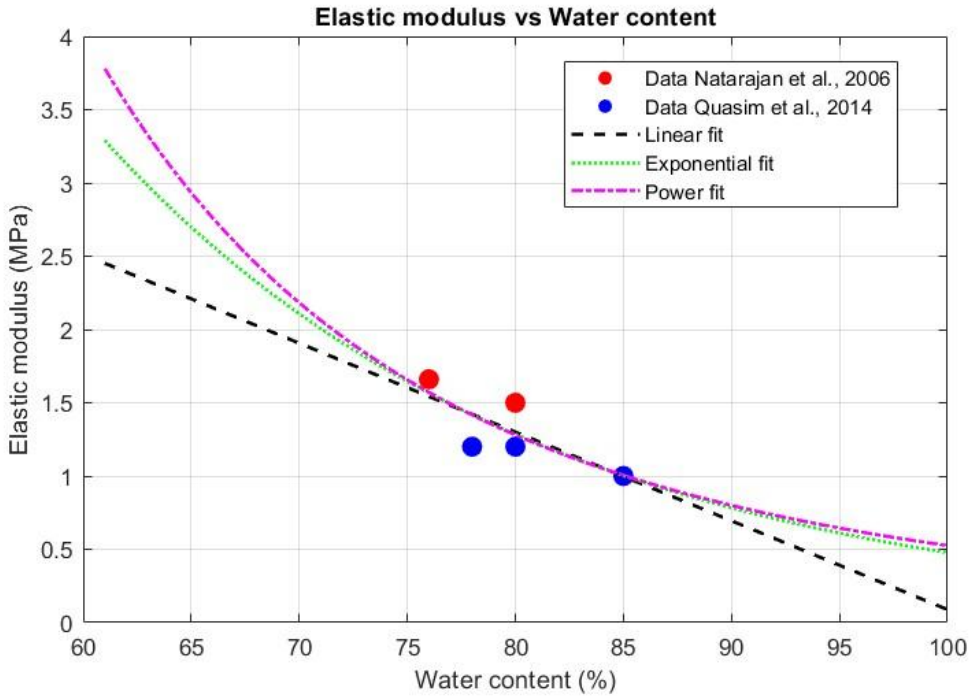

Figure 27:Fitting Models for the Relationship Between Water Content and Elastic Modulus

Exponential fitting was the best fit to the data and hence was chosen as the final report:

$$E = 67.39 * e^{(-\%W.C.*0.0495)}$$

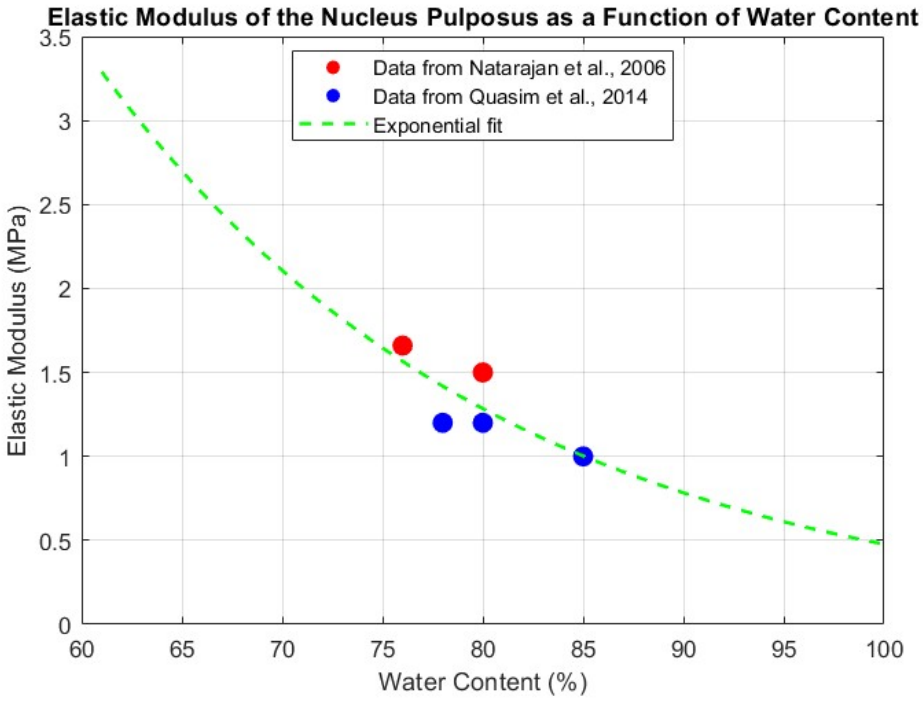

Figure 28:Elastic Modulus of the Nucleus Pulposus as a Function of Water Content

where E is the elastic modulus in MPa and W.C is water content as a percentage.

The resulting curve displays increase of the elastic modulus with decreasing hydration: at 85% water content, for example, the modulus is of the order of 1 MPa; at 80%, of the order of 1.5 MPa; and well above 2 MPa when water content is reduced to 76%. These figures are in keeping with the experimental data from which the curve has been developed [50], [54]. The curve was subsequently fitted to water content values determined from MRI images of segmented discs. In the discs in which the nucleus was still visually discernible (T9–T10 and T12–L1), the elastic modulus was especially applied to the nuclear region, according to the calibration relationship established.

This method allowed us to estimate subjectively and physiologically the elastic modulus of the nucleus pulposus, starting from the hydration values obtained from the MRI images, and thus obtaining a mechanical characterization for each disc analysed [52], [53].

2.6.3 Quantitative Estimation of Nucleus Pulposus Compressibility and Poisson's Ratio

Based on the estimation of the elastic modulus of the nucleus pulposus from a calibration curve with respect to the water content as described above, it was possible to determine the corresponding Poisson's ratio. This parameter is required for the characterization of the mechanical behaviour of the nucleus pulposus because it characterizes its tendency to expand in the transverse direction when compressed axially. The Poisson's ratio is a direct indicator of tissue compressibility and is related to the state of degeneration of the intervertebral disc (IVD) [53], [56].

In order to estimate Poisson's Rate (ν), one not only must be aware of the elastic modulus E, but also of the compressibility B (the bulk modulus's reciprocal), since it quantifies the resistance of the material to volumetric deformation. The theoretical relation utilized in this work for the calculation of the Poisson's ratio, between E and B, is given by the following equation:

$$v = \frac{1}{2} * \left(1 - \frac{E * B}{3}\right)$$

This relation, used in Wilson et al (2005) [56] to simulate the soft hydrated tissue such as IVD and cartilages, enables a estimation of Poisson ratio from known mechanical quantities.

While the elastic modulus E was derived from water content through the calibrating curve, the compressibility B was approximated through similar procedure. That is, data from Parke et al. (2013) were employed, which establish high linear correlation between percentage loss of disc height - use as marker for degeneration- and NP compressibility [57]:

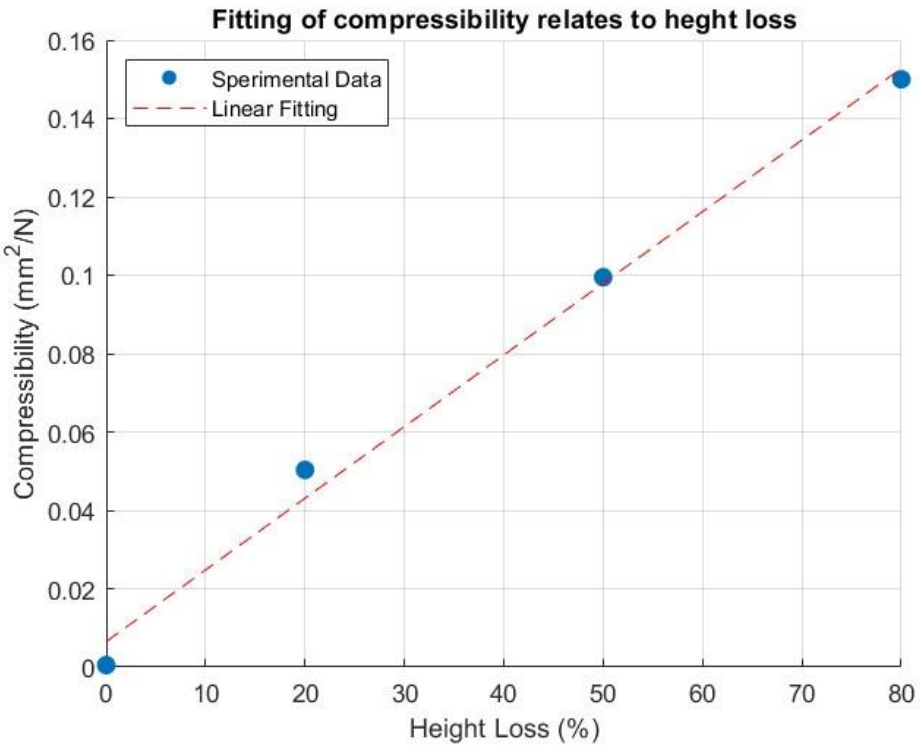

Figure 29: Fitting of compressibility

$$B = 0.001829 * \%H.L + 0.006506$$

Where the B is the compressibility and %H.L. is the percentage of the height loss of the discs. This curve is used to estimate the compressibility of the T9/T10 and T11/L1 nucleus of the model (Table 12).

Nucleus	*Height value*	*Normal height (Frost e.la. 2019)*	*%H.L.*	*Compressibility (B)*
T9/T10	4.989 mm	4.90mm	Healthy (0%)	$0.0065\frac{mm^2}{N}$
T12/L1	5.730mm	6.80mm	Moderate (15%)	$0.0335\frac{mm^2}{N}$

Table 10 : results from calibration curve of compressibility

Once both E and B were obtained, Poisson's ratio was calculated from the above formula.

Thanks to this strategy, a realistic and subject-specific prediction of the mechanical behavior of the nucleus pulposus was possible, taking into account its elastic and volumetric response with respect to the hydration state. This allowed for a more realistic description of the tissue reaction to physiological loading, paving the way for more realistic and subject-specific biomechanical simulation.[53], [56].

2.7 Biomechanical Characterization of the Annulus Fibrosus

Annulus fibrosus is an important structural component of the intervertebral disc, made up of alternately oriented concentric lamellae that are mechanically robust in multiple directions. Its response has been indicated to be anisotropic and nonlinear with properties varying based on anatomical location (anterior, posterior, inner, outer) and direction of load. The FEM emulates this complexity using the widespread application of hyperelastic constitutive models, such as the Mooney-Rivlin model, which are able to accurately represent the mechanical behaviour of the AF under large deformation [58].

Different approaches have been proposed in the literature for defining the material properties of the AF. In some studies, mechanical properties of the annulus are assumed to be constant regardless of the degree of disc degeneration. Rohlmann et al. 2006 [59] simulated disc degeneration by altering the discal geometry and the bulk modulus of the nucleus, whereas annulus was kept unchanged. In the same way, Bin Zhang et al. (2025) [60] used constant Mooney-Rivlin parameters for the annulus in all degeneration grades. Conversely, other studies offered mechanical properties related to discal degeneration. Ruberte et al. (2009) [61] used increasingly increasing value of the Mooney-Rivlin parameters C1 and C2 for the AF, between 0.2/0.05 for healthy tissue and 0.9/0.23 for moderate degeneration. This corresponds to progressive stiffening of the anulus with dehydration and degeneration. The same strategy was also used by Caie et al (2020) [62] and DU et al. (2021) [58], who all simulated both material and geometrical changes to simulate a real degenerative state. In addition to this, recent research such as Coombs et al. (2017) and Gruber et al. (2024) has highlighted a great necessity of adequately portraying the spatial and subjective heterogeneity of the annulus using more advanced constitutive such as the anisotropic Holzapfel-Gasser-Ogden (HGO) model. In demonstrations by Coombs et al., fibre angle and stiffness parameters were shown to play a significant role in the mechanical response of the vertebral segment. Gruber et al. further proved that the HGO model may be calibrated more accurately than structural rebars-based models with high computational efficiency.

In the present study, the fibrous annulus was modelled using the two-parameter Mooney-Rivlin hyperelastic model. The values of the C1 C2 coefficients were determined from calibration curves extrapolated from the biomechanical literature. The compressibility parameter D was instead kept constants for all the discs, in line with what has been proposed in other FEM studies

and engineering theses that adopt this simplification. The decision to use the Mooney-Rivlin model, than the more advanced Holzapfel-Gasser-Ogden (HGO) formulation, was made in an attempt to adopt a computationally less demanding and less calibrated approach. Although the HGO model presents a better description of the anisotropy of the fibrous annulus, the Mooney-Rivlin model was adequate to represent the mechanical tissue behaviour under large deformation, especially in situations where access to experimental data is limited. The choice also facilitated easier incorporation of the model in the medical image-based workflow. In this model, the case of the severely degenerated discs T10-T11 and T11-T12, an additional simplification was made: the whole disc was simulated by assigning the mechanical behaviour of the fibrous annulus to the whole structure. The rationale for this is that, in the case of advanced degeneration, the nucleus pulposus loses its structural and functional properties, taking on annulus-like features [63], [64].

2.7.1 Assignment of Mooney-Rivlin Parameters to the Annulus Fibrosus

This section describes in detail the process used to assign the mechanical parameters C1 and C2 in the Mooney-Rivlin hyperelastic model, employed to simulate the behaviour of the annulus fibrosus (AF) at levels T9–T10 and T12–L1, and the IVDs at levels T10–T11 and T11–T12, which were fully simulated from the mechanical properties of the AF. During the first phase, also the compressibility parameter DDD of the volumetric compressibility of the material was considered. However, for simplicity—and according to other FEM texts—it was decided to keep this parameter constant for all models [65].

Mooney-Rivlin model is a hyperelastic constitutive model widely used to describe the nonlinear behaviour of soft tissues subjected to large deformations. It is expressed based on a strain energy function that depends on the invariants of the Cauchy-Green deformation tensor and is described by two main parameters: C1, the dominant contribution to material stiffness, and C2, controlling the curvature of the mechanical response [46], [65].

In this work, the choice of this model was driven by necessity directly by the intention of having an appropriate depiction of the mechanical behaviour of the annulus fibrosus (AF) and making the numerical framework as simple and effective as possible in order to be implemented easily in geometric models based on medical images. Also, it was noted that values of the parameters

C1 and C2 indicated in the literature differed based on the state of degeneration of the disc. In contrast to the nucleus pulposus, where water content could be used as a direct measure of degeneration, this was not possible with the annulus fibrosus. There is no significant correlation between the mechanical state of the annulus and water content, as many studies have shown. Loss of intervertebral disc height typically, a geometric parameter directly measurable from images, is more correlated with anulus structural degeneration.

Based on this observation, it was resolved to adopt the disc height loss as a reference variable for calibrating the mechanical parameters of the annulus. Herein, several scientific articles were consulted in which values for the Mooney-Rivlin model's parameters C1 and c2 had been given corresponding to different grades of disc degeneration, usually expressed as percentage height loss relative to a control disc. To be precise, information from the articles of Ruberté et al. (2009) [61], Cai et al. (2020) [62] and Du et al. (2021)[58] were used to develop the calibration curve for C1(Figure 30).

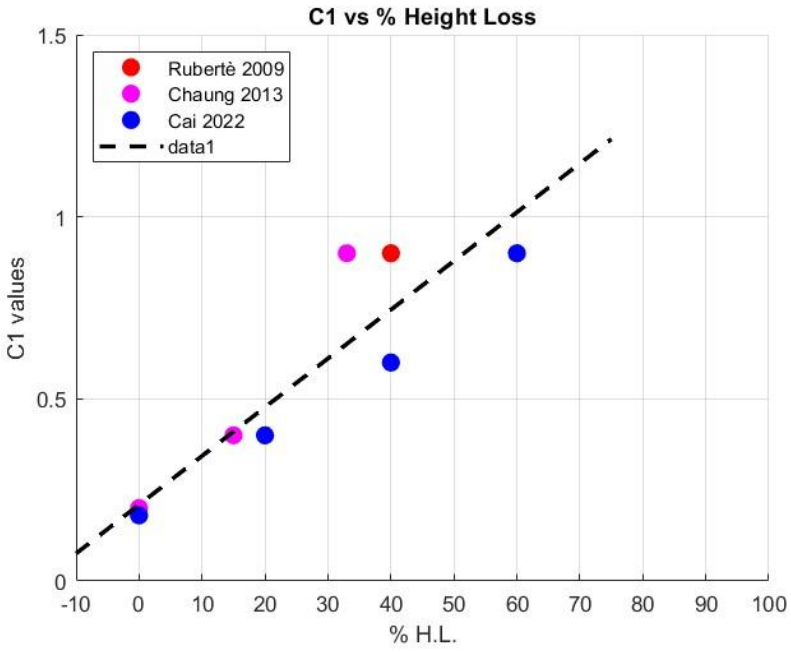

Figure 30: C1 parameters related to height loss

$$C_1 = 0.01339 * \%H.L + 0.2095$$

for parameter C2 calibration, nevertheless, articles of Ruberté et al. (2009) [61], Cai et al. (2020) [62] and Chang Liang et al. (2025)[66] were used (Figure 31).

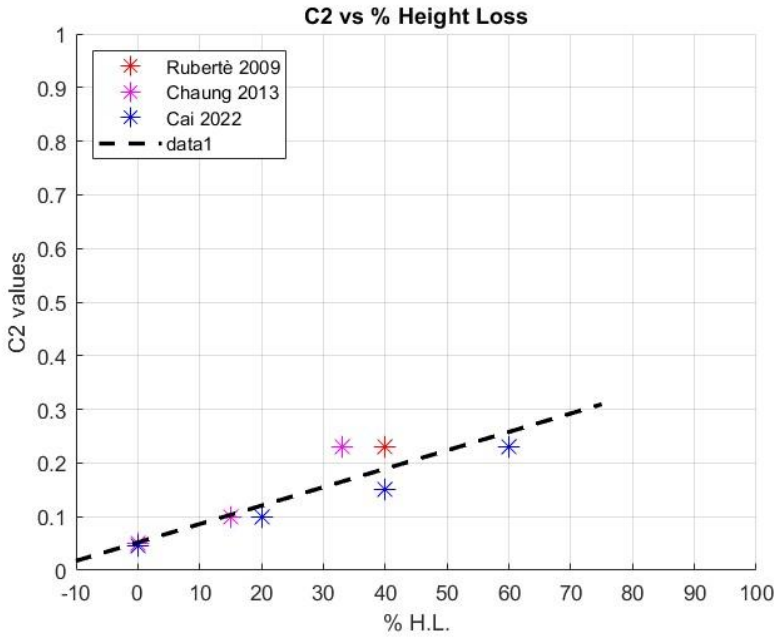

Figure 31: C2 parameters related to percentage of height loss

$$C_2 = 0.003434 * \%H.L + 0.05191$$

Upon these two curves having been defined, they were used to compute the C1 and C2 parameters that would be utilized for our discs. More specifically, in each of the segmented discs, from the MRI scans directly, the height reduction percentage compared with a normal reference was measured. These were input into the previously computed calibration curves, and the respective C1 and C2 parameters were objectively and automatically calculated.

Therefore, the mechanical parameters of the annulus fibrosus could automatically and directly be linked to the morphological conditions within the MRI images, and a characterization was achieved that not only shows the degree of degeneration of each disc but also follows the anatomical specificity of the subject. This approach therefore offers a solid and flexible basis for use in personalized biomechanical models.

2.8 Creation of FEM model

Construction of the Finite Element Model is a fundamental operation in creating a computational system for biomechanical simulation of the spine. It is based on the geometric discretization of the anatomical components—vertebrae and intervertebral discs—into a finite number of elements, typically of tetrahedral or hexahedral shape. Each of the elements is designed to be governed by the equations defining the mechanical behaviour of the biological tissues [67], [68]. The FEM model is the core of numerical simulations, typically carried out through special software tools allowing the evaluation of stress distribution, deformations, internal pressures, and other biomechanical parameters for physiological or pathological loading conditions [24], [30]. Model generation typically starts from CT or MRI scans, where the 3D surface of the anatomy of interest is reconstructed. After geometry acquisition, one must move to mesh generation, i.e., the division of the volume into small finite elements. This can be done in a few ways: structured meshes show a regular grid, whereas unstructured meshes fit the complexity of the anatomical geometry. The elements might also be hexahedral—more accurate but harder to map into complex shapes—or tetrahedral, which are more general and therefore common in patient-specific models [29], [67].

The type of elements used to represent the geometry can be varied. Two-dimensional (2D) elements such as quadrilateral (quads) and triangular (trial) elements are used for coarse meshing or in a structure whose one dimension is small. In 3D models, the main element types are tetrahedra (Tetra), prisms (Penta), hexahedra (Exa), and pyramids. All these are used to fulfil individual modelling needs based on geometry and simulation needs. The choice of the kind of element depends on the physical model under consideration and the result to be achieved via the simulation [69]. Another important parameter is mesh density, which varies with the region of anatomy and level of precision to be achieved. Higher density mesh, which has more elements, improves resolution and reliability of results but also the cost of computation. Additionally, it can be combined with homogeneous meshes, where elements are of equal magnitude throughout, or heterogeneous meshes, where higher resolution is used where there is mechanical interest.

In the present study, the .STL files generated in 3D Slicer were then imported into Altair HyperMesh, a pre- and post-processing finite element analysis tool. HyperMesh is particularly adept at working with complex and high-definition models and was utilized for the generation of the 2D surface mesh and the final 3D vertebrae and intervertebral disc mesh. The software

offers full control over mesh topology, element type, and refinement strategy. In spinal biomechanics, FEM models are employed to analyse a range of research and clinical scenarios: evaluation of load transmission under static or dynamic conditions, simulation of intervertebral disc behaviour with degeneration, fracture risk prediction, and prediction of surgical outcome. With the increasing accessibility of imaging techniques and dedicated modelling software, use of FEM models is increasingly being applied in clinical research studies, engineering design, and biomedical simulation environments.

2.8.1 Vertebral Mesh Generation

Meshing of the vertebrae is a very important step in the construction of FEM models since it has a direct impact on the simulation accuracy of biomechanics. The vertebrae present a very complicated geometry with the articular, spinous and transverse processes, and the irregular curvatures and axes of symmetry that are hard to define. For this reason, the mesh generation was carried out separately for each vertebra, with the hope of locally enhancing the discretization quality and adequately address critical regions such as the posterior arches. The 3D geometry models of the vertebrae, segmented from the CT images in 3D Slicer and saved as STL files, were imported into Altair HyperMesh, where a first surface mesh (2D) was formed, consisting of triangular 'trial' elements, with an approximate size of 1 mm. This surface mesh formed the basis for developing the 3D volumetric mesh, which was built with 10-node quadratic tetrahedral elements (Figure 32).

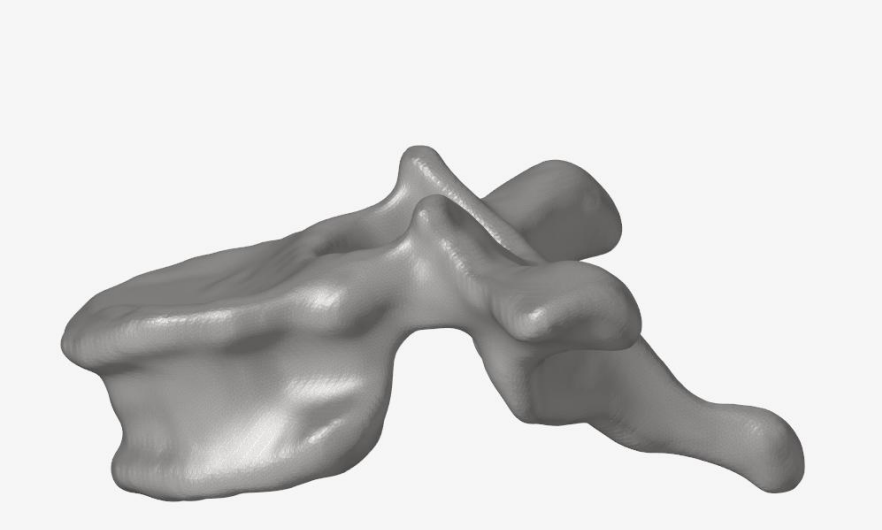

Figure 32: File.STL of T9 vertebrae

The choice of tetrahedral elements is excused due to their geometrical flexibility and ease of fitting into irregular geometries. In addition, C3D10 elements offer the potential for more accurate representation of curvatures and greater numerical stability than linear tetrahedral elements, even though they entail an increase in the number of degrees of freedom and thus the computational effort [67], [70]. Overall, the increased accuracy justifies the use of this element type, especially in subject-specific contexts where high geometric fidelity is essential (Figure 33).

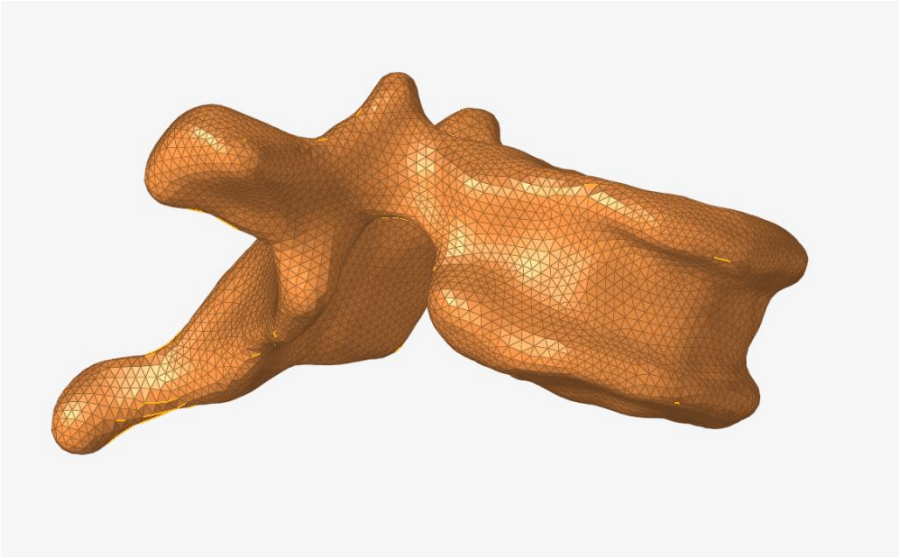

Figure 33:Triangular Surface Mesh of a Thoracic Vertebra

The same procedure was applied to all the vertebrae of the T9-L1 tract, generating an independent tetrahedral mesh for each, which was subsequently joined to the other model components. Particular attention was paid to the correct connection between vertebrae and adjacent intervertebral discs. In the case where the discs were modelled with hexahedral elements, it was necessary to carry out an equalisation operation of the corner nodes, so as to obtain continuity between the meshes and guarantee realistic load transmission without having to define contact surfaces (Figure 34).

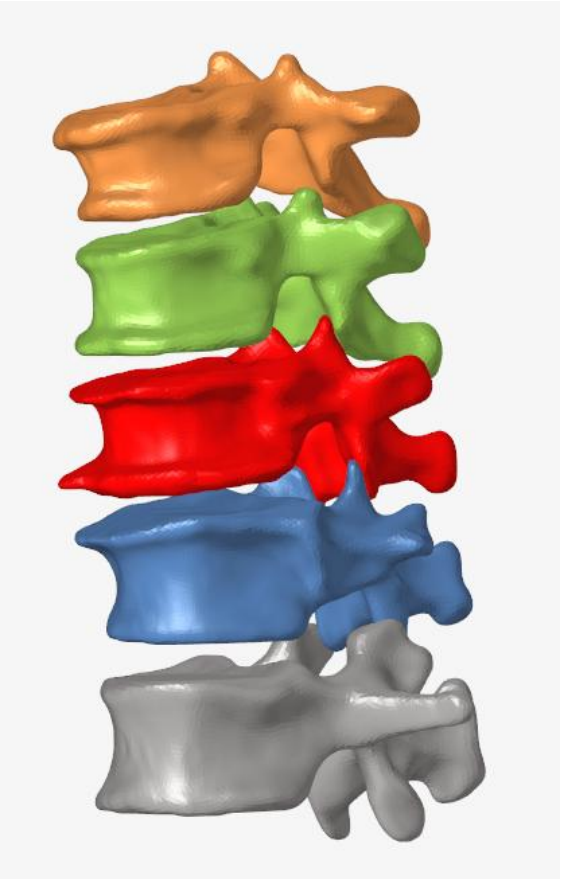

Figure 34: Final model of vertebrae (T9-L1).

2.8.2 Mesh creation of intervertebral discs

The modelling of the intervertebral discs was dealt with differentially depending on the morphological state observed in the MRI images. In the case of a degenerate disc where the internal structures of the disc could not be readily identified, a whole-disc mesh was generated and modelled as a homogeneous block. On the other hand, for discs in which it was possible to distinguish the nucleus pulposus (nucleus pulposus) and the fibrous ring (annulus fibrosus), a separation of the two parts in two distinct meshes was opted for, in order to more closely represent the morphological and mechanical difference between the two tissues. This also required the use of a different meshing method for each compartment, as described in the following paragraphs.

2.8.2.1 Creation of the hexahedral mesh of the annulus fibrosus

The AF was modelled using a three-dimensional mesh of hexahedral elements, which are particularly well adapted to describe the lamellar structure of the fibrous ring and for the treatment of hyperelastic or fibrillar-oriented material. The starting point was, as with the vertebrae, the STL file resulting from the segmentation of MRI images within 3D slicer (Figure 35).

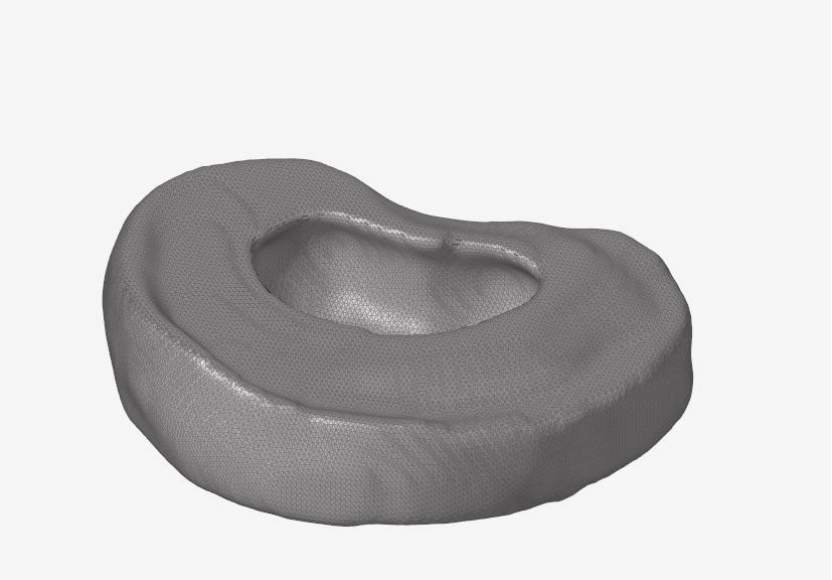

Figure 35: File STL of annulus fibrosus

After importing in Hypermesh, a 2D surface mesh was created, with elements being of quadrilateral type ('quads') with an average dimension of 1 mm (Figure 36). Then all the elements of the top portion were selected from this surface mesh to construct the top face of the disc. On this surface, particular attention was paid to how the elements were positioned, striving to achieve as concentric a mesh as possible, to accurately simulate the circular arrangement of the lamellae that make up the annulus. Subsequently, the upper face of the disk was dealt with, selecting the corresponding elements to generate the upper face from where three-dimensional modeling would be commenced.

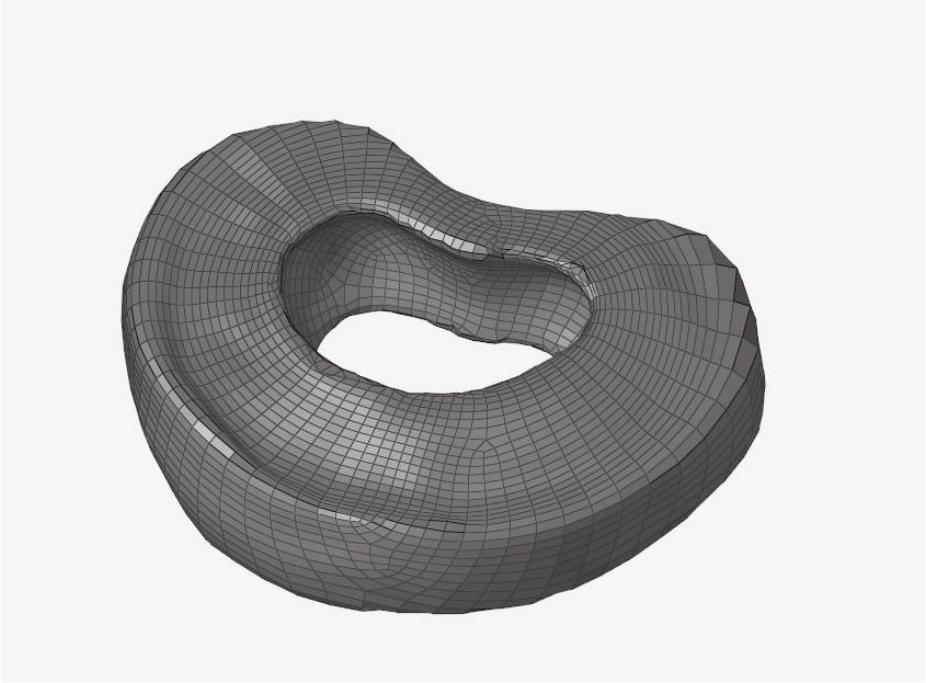

Figure 36: 2D mesh of annulus fibrosus

In this case, the top face was projected onto the horizontal plane using the *Topology → Align/Project* command and then translated into a surface using *2D → Surface → From FE*. The original elements were removed, and the resulting surface was subdivided-ready. This was then graphically subdivided into equal zones using *Topology → Lines* and drawing guides that were later used to subdivide the surface using *Topology → Split/Stitch → Split-Interactive*. Each of them was turned into a single surface with *2D → Surfaces → Patch/Spline* and collected into a new component. A concentric mesh was defined for each of them with the *2D → MapMesh* command (parameters: Element Type: Quads only; Map Type: Rectangle),

changing the density so that they were evenly spaced. After completion, the surfaces were removed and a 2D mesh of the annulus with elements in a concentric arrangement, which mirrors the organization of the lamellar tissues (Figure 37).

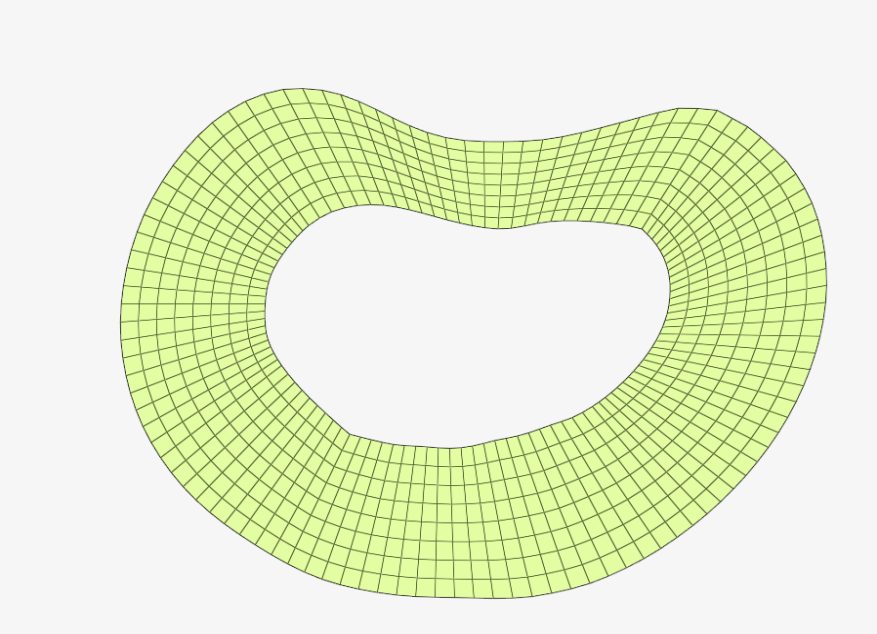

Figure 37: concentrical mesh of superior face of AF

To fit this mesh to the articular surfaces of adjacent vertebrae, *morphing* was then performed between the top surface of the disc and the bottom surface of the superior vertebra, and the reverse between the bottom surface of the disc and the top surface of the inferior vertebra. Mesh morphing, the process of altering the shape of a mesh by directly altering the nodal co-ordinates

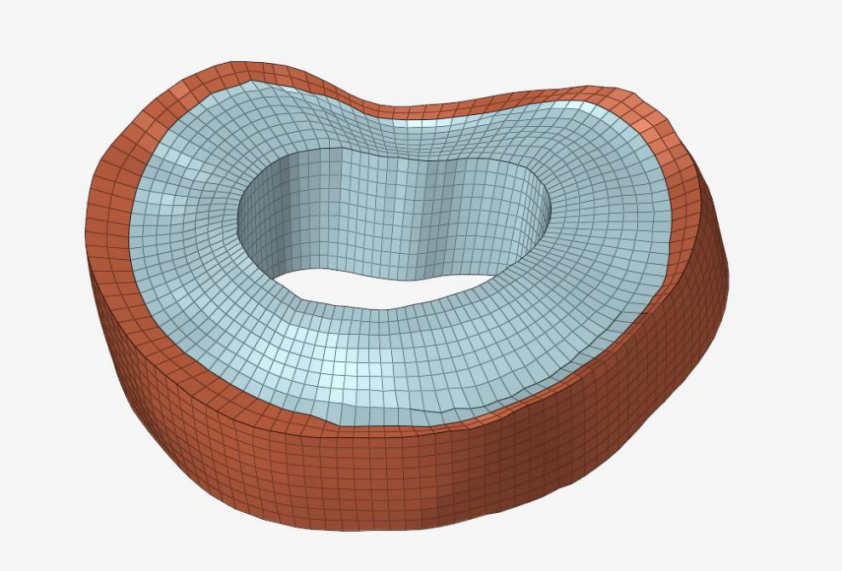

Figure 38: Final models of AF with external bulge

without modifying the connectivity, is being used very intensively in FEM to get good geometric fits [71]. After these operations, a *solid map* was done between the two deformed surfaces, obtaining an initial version of the volumetric mesh of the annulus (Figure 38).

To correctly represent the external shape of the annulus, a bulge was then created, constructed from the actual segmentation. The elements of the first solid map were selected and, simultaneously, those of the bulged segmentation. Morphing between the two populations resulted in a geometry consistent with the anatomical shape of the disc contour. Finally, another solid map was used between the morphed bulge and the initial one to complete creating the three-dimensional hexahedral mesh of the annulus fibrosus.

2.8.2.2 Creation of the hexahedral mesh of nucleus pulposus

After we had completed the modelling of the annulus fibrosus, we went on to construct the nucleus pulposus, at once making utilization of the geometry already accomplished of the annulus. That is, the internal parts of the annulus bulges were utilized, i.e. that innermost central portion which in anatomical reality is the portion of the nucleus (Figure 39):

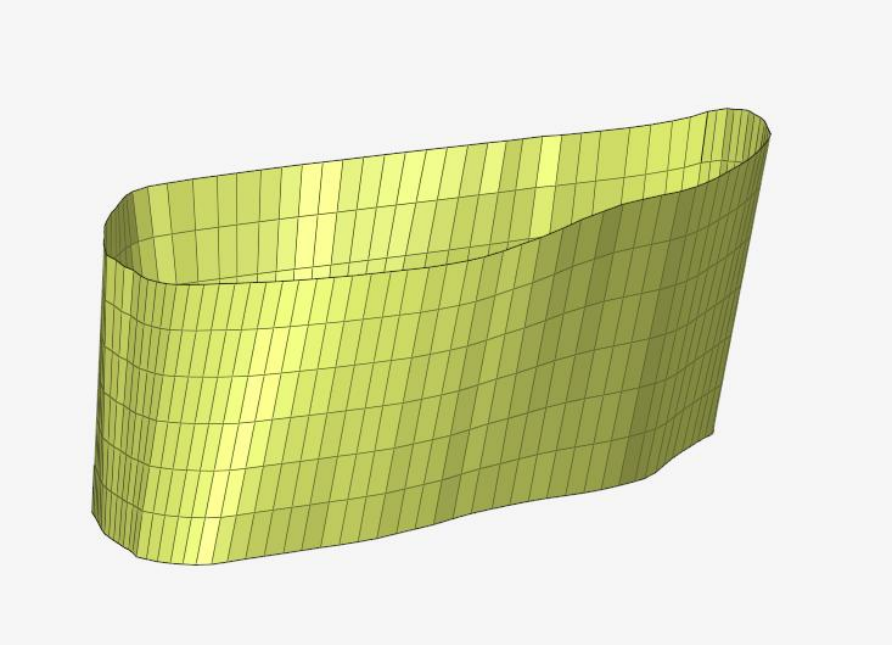

Figure 39: Internal Buldg of AF

After this internal bulge was extricated, the top and bottom of the volume were closed, using the Fill Hole option, to produce a solid. At this point, in an attempt at both geometric and anatomical continuity with the nearby vertebrae, it was resolved to shape the top and bottom surfaces of the internal bulge into conformity with the bottom surface of the upper vertebra and the top surface of the lower vertebra, respectively (Figure 40).

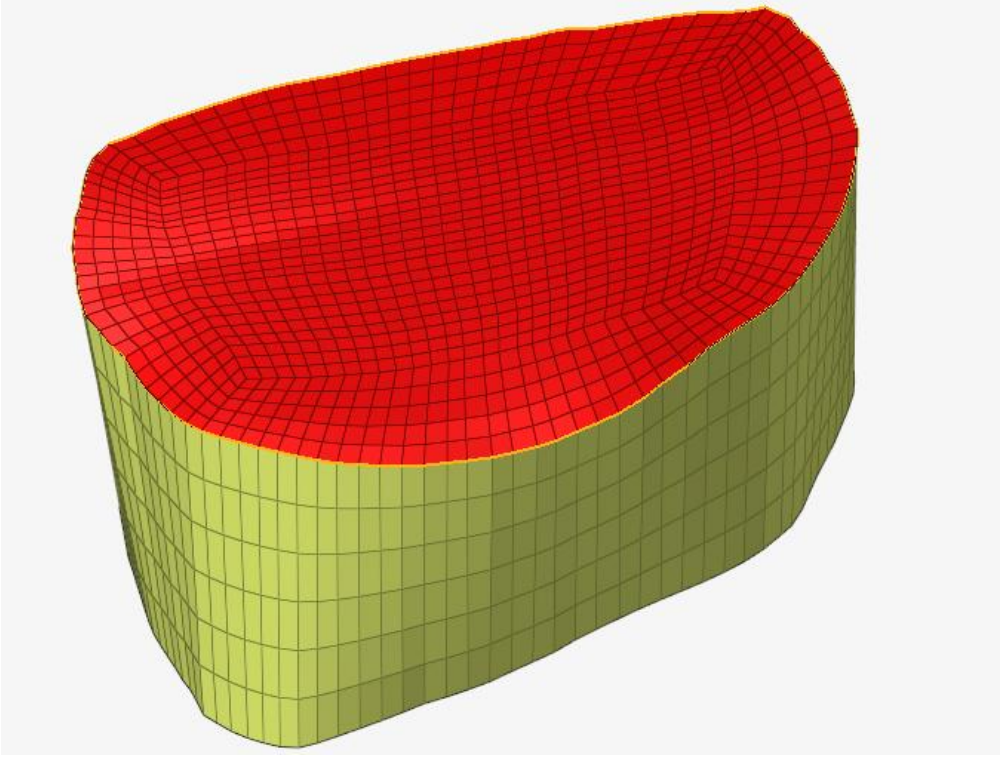

Figure 40: mesh of superior face of NP

Then the mesh was formed, with a concentric design of the elements to mimic the geometric design according to the inner disc tissues. Secondly, the bottom nucleus surface was selected, and further morphing was performed relative to the top surface with the purpose of having the same shape as the top surface but with the same elements and node number of the bottom surface. This was due to the need for maintaining the surfaces in correspondence to facilitate volume generation. Also, the *MoveToFree* function was utilized to position the nodes exactly coincident at the boundary between the inner bulge and the surrounding surface. This command was able to shift the nodes exactly and make them turn perfectly coincident, thus forming a continuous connection between all the parts of the model, both geometrically and in terms of the mesh.

Lastly, the *SolidMap* operation was run between the already transformed surfaces, thus generating the resulting three-dimensional model of the nucleus pulposus, fully incorporated into the anatomical setting of the intervertebral disc (Figure 41).

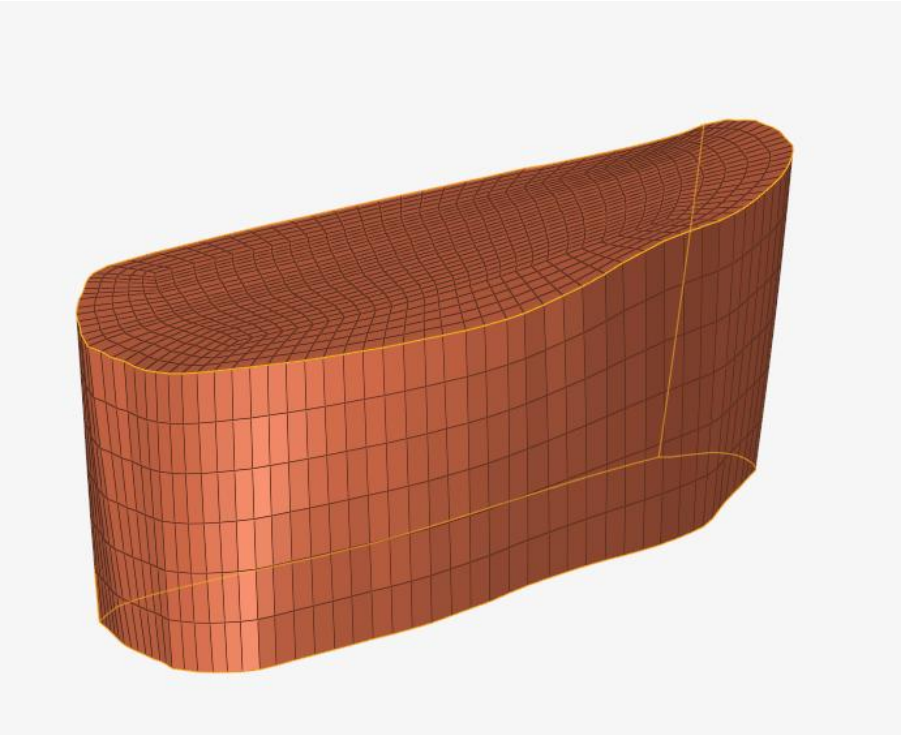

Figure 41: Final model of NP

2.8.2.3 Creation of the hexahedral mesh of IVD

In the degenerated intervertebral disc, the nucleus pulposus could not be differentiated from the annulus fibrosus. For this reason, it was resolved to model the whole disc as one structure, with a similar modelling process to that for the annulus, but with some difference in the initial phase (Figure 42).

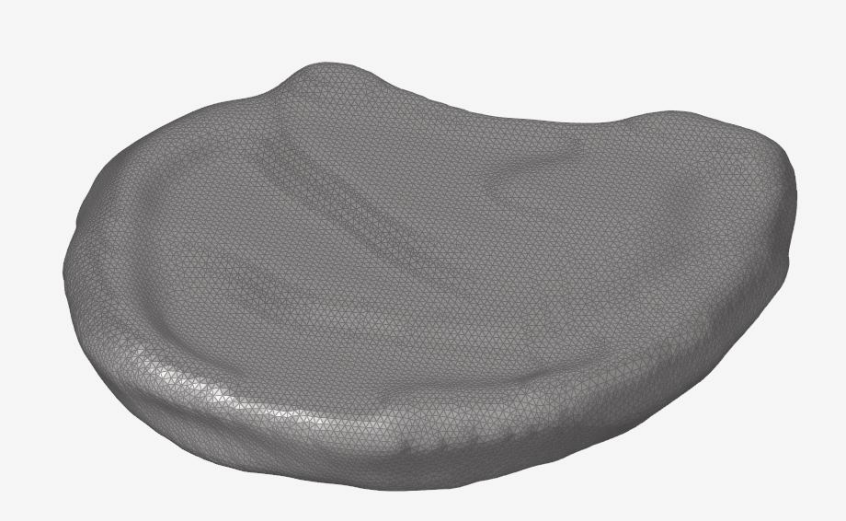

Figure 42: file.STL of degenerated disc

The meshing process to create the mesh continued with the same preliminary steps that had been used for the other discs heretofore: importing the STL file created with segmentation into HyperMesh and initially mesh the model in 2D.

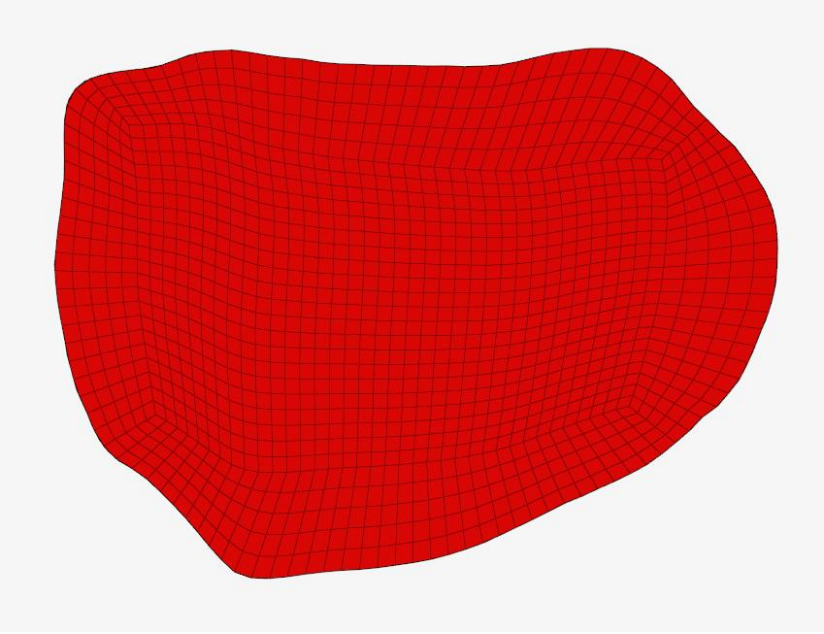

Figure 43: concentric mesh of the upper surface of the disc

Next, the upper face of the disc was worked on. After selecting the elements of this section, the *Mesh as Circle* command was applied. This tool allowed one to create a concentric pattern of the elements in the peripheral region, which should occupy the space of the organisation of the AF, and a more organised and rectangular mesh in the intermediate region, which took up the space that was once occupied by the now unrecognisable nucleus. This was a design where in certain compatibility with the physiological anatomy of the disc was preserved but modified to accommodate the restrictions imposed by degeneration (Figure 42).

After the acquisition of the upper face, the rest of the process was identical to the one explained for the annulus fibrosus. The upper face was copied and deformed to get the lower face, which was morphed with the surface of the vertebra below, in the same way the upper face was morphed with surface of the vertebra above. The intermediate volume was closed using a solid map, leading to an initial 3D hexahedral mesh. To close the geometry and precisely match the anatomical form of the degenerate disc, the peripheral bulge was ultimately modelled from the real segmentation. Morphing the solid map mesh and the segmented bulge allowed for reconciling the two geometries. After this process, the second solid map was used between the bulge after morphing and the original bulge, thereby creating the final mesh of the degenerate disc, ready for material assignment and integration into the complete FEM model.

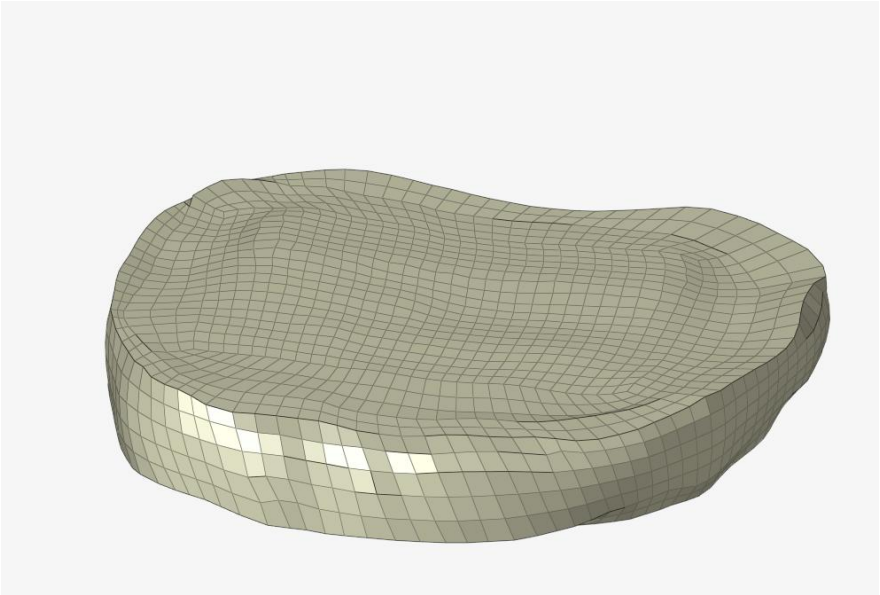

Figure 44: Final model of IVD

2.8.2.4 Cut and Stitch Technique for Mesh Integration

After meshing the vertebrae and the intervertebral discs, an additional step was required to provide continuity to the FEM model, considering that the discs had been meshed using hexahedral elements, whereas vertebrae had been discretized with tetrahedral elements. Since the two meshes have different types of elements, it is not possible to join the volumes directly while maintaining nodal coherence, so a surface fitting and matching procedure had to be carried out. Thanks to the morphing procedure performed earlier, the disc and vertebra articular surfaces already matched perfectly. We exploited this geometrical coincidence by picking the nodes of the top (or bottom) face of the disc, and gave a split command, splitting the quadrangular elements (quads) of such a face into triangles. This generated a new surface to match the vertebra tetrahedral mesh. Now, that new triangular face obtained due to the division was defined as the new face of the vertebra, instead of the original part.

Connection operation was then performed between the new face and the rest of the vertebra by a connection command, which allowed for restoring continuity of vertebral mesh without needing to start from a new geometry. This approach enabled the retrieval of a continuous del, free from interfaces or artificial contact surfaces, and provided for continuous load transmission between vertebrae and discs (Figure 45).

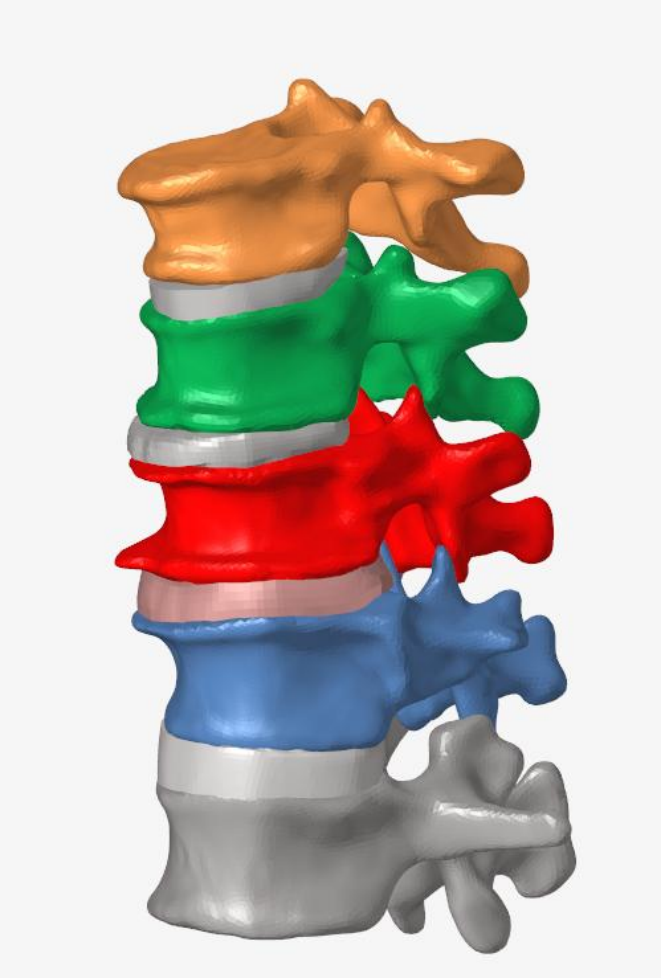

Figure 45: Final model of the entire trat T9-L1

Chapter 3

Discussion and Results

3.1 T_2 Relaxation Time Estimation in Human Intervertebral Discs

One of the main goals of this work was to measure the T2 relaxation time of IVD to non-invasively assess their state of hydration. The T2 parameter, obtained by the MRI, is related to the interaction between the water molecule and the extracellular matrix: when the water content is greater and in the surroundings there are high levels of proteoglycans, as in the IVD, the T2 values are higher; while in the degenerated disc, where there is a dehydration phenomenon, the T2 values are lower [72], [73], [74]. Since a multiple echo sequence was not performed in this present study, a numerical method was applied to estimate T2 from a lone TE of 108,432 ms. To counteract the lack of more than one signal decay points, an algorithm from simulated annealing method was applied in Matlab. This algorithm finds the best T2 value by iteratively reducing the difference between an observed signal intensity and the exponential decay model. The calculated T2 values conformed to expectations: T9/T10 and T12/L1 had mean T2 values of 110.9 ms and 113.5 ms, respectively, with low standard deviation, reflecting good hydration. On the other hand, T10/T11 and T11/T12 had lower T2 values that reflected the lesser water content and structural deterioration. These findings are entirely consistent with data report in human research: Chiu et al. (2001) [72] recorded T2 values of approximately 115 ms in normal discs and less than 60 ms in severely degenerated ones. Similarly, Alkalay et al. (2015) [73] and Drake-Perez et al.(2019) [74] found progressive decreases in T2 with increasing Pfirrmann grade. In the disc where NP and AF were separable (T9/T10 and T12/L1), regional variation in T2 was observed, the NP greater values than the degenerated discs. This is physiologically reasonable as the NP contains more water. These variations further demonstrate sensitivity of the method used even when applied to single - eco data. Clinically and biomechanically, the apparent discrimination between T2 values of healthy and degenerative discs follows known patterns of degeneration. Virk et al. (2021) [75] showed that higher Pfirrmann grades relate to

reduced disc failure load and lower disc height- consistent with the morphological and functional findings within this study. In addition, Zhu et al.(2017) [76], with the simulation on the IVD, confirm that the water content in the NP is decreased by over 15% in degenerated situations directly impacting spinal biomechanics (Table 11).

Table 11: T2 relaxation Time

Structure	*T2 values*	*Standard Deviation*
IVD T9/T10	110.9 ms	9.95 ms
IVD T10/T11	48.82 ms	8.99 ms
IVD T11/T12	53.66 ms	9.95 ms
IVD T12/L1	113.49	6.87 ms
Nucleus T9/T10	91.52 ms	10.24 ms
Annulus T9/T10	79.2 ms	10.91 ms
Nucleus T12/L1	84.56ms	10.75 ms
Annulus T12/L1	85.70 ms	6.08 ms

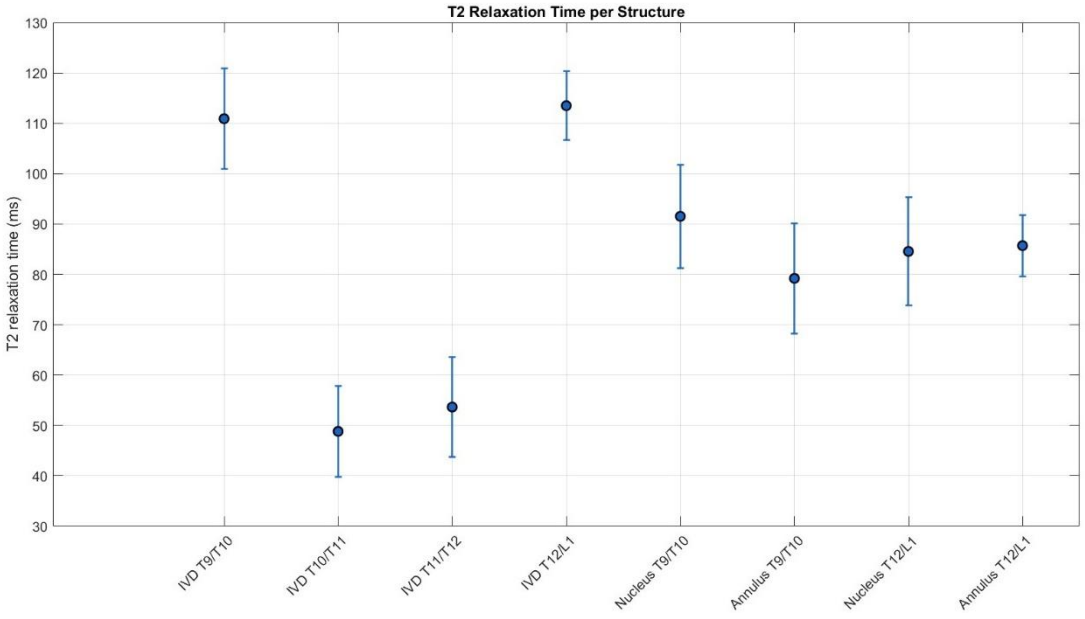

Figure 46: Mean T2 values and standard deviations in intervertebral discs and their components

Figure 46 graphically presents the mean values of T2 for each structure examined, along with the respective standard deviations. In addition to visually confirming the apparent difference

between normal and degenerated discs already explained in *Table 16*, the graph also enables one to immediately visually appreciate the intra-structure variability. Particularly, a lower dispersion of values is observed in the healthy discs (T9/T10 and T12/L1), which means higher homogeneity in the distribution of water content and a better-ordered tissue organisation. Degenerated discs (T10/T11 and T11/T12) are more variable, perhaps representing extracellular matrix disorganization and localized loss of hydration. A further important feature that the figure highlights is the capacity, in non-degenerate discs, to distinguish between annulus fibrosus and nucleus pulposus and represent the difference in T2 terms. The nucleus, as expected, is seen to have higher T2 values than the annulus, consistent with the higher physiological water content. This regional discrimination not only validates the biological reality of the segmentation performed but also testifies to the sensitivity of the approach used in detecting local differences, even with the use of data acquired with a single echo.

Therefore, the procedure proposed supported reliable estimation of T2 in human IVD with results consistent with known physiological and pathological changes. These values will serve as the reference for water content estimation as well as for subject-specific mechanical properties assignment.

3.2 Results and discussions of estimation of Water content

In the present study, the water content is estimated indirectly from the T2 values obtained from the simulated annealing algorithm. For the conversion from T_2 to percentage water, two different calibration curves were applied. The first curve is based on the article by Marinelli et al. (2009) [44], who studied the relationship between T_2 and water content on human intervertebral discs, proposing a linear shape relationship. This curve, widely cited in the literature, has been used in numerous studies to estimate water content from T_2-weighted images. To improve the estimation, a mixed calibration curve was therefore also used, combining the data of Marinelli et al.(2009) [44] with those of Weidenbaum et al. (1992) [48]. The latter study was conducted on human disc samples. The combined curve provided another, more refined estimate of the water content in discs under different degeneration conditions (Table 12).

Table 12:Water content results

Structure	*T2 (Ms)*	*%W.C (Marinelli 2009)*	*%W.C (Marinelli 2009 with Weidenbaum 1992)*
NP T9/T10	91,52 ms	79,46%	77,15%
NP T12/L1	84,56 ms	77,45%	74,07%
AF T9/T10	79,2 ms	75,90%	71,69%
AF T12/L1	85,70 ms	77.78%	74.57%
IVD T9/T10	110.9ms	85.7%	84.6%
IVD T10/T11	48,83 ms	58,29%	67,14%
IVD T11/T12	53,66 ms	60,38%	68,51%
IVD T12/L1	113.49ms	86.8%	85.34%

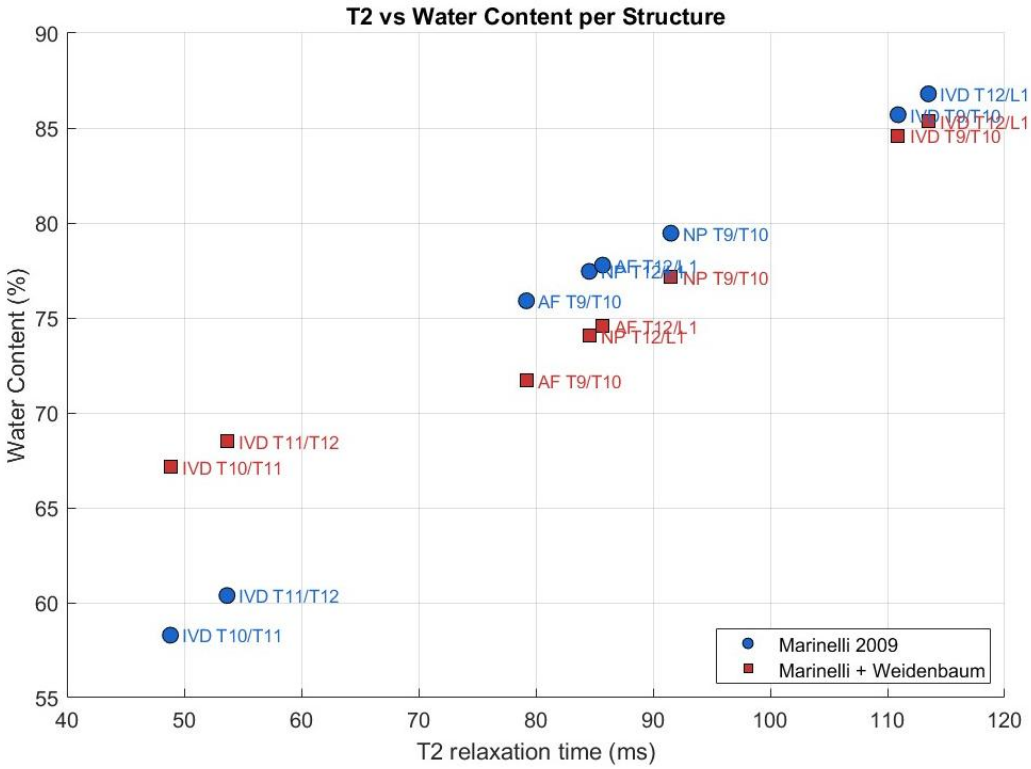

Figure 47: results of water content with two different calibration curve

Figure 47 is a representation of the distribution of water content data versus T2 relaxation time in scatter plot form for all the structures that have been analysed. In addition to showing the high correlation between both variables, the plot clearly illustrates the discrimination between discs that have been classified as healthy and degenerated, highlighting how low T2 values map consistently with decreasing percentages of water. This visual consistency also aids the credibility of calibration curves used, leading to a pathophysiological image in agreement with evidence reported in the literature. The fact that there is also a slight difference between the two curves (Marinelli and combined with Weidenbaum) shows how both deliver a credible view of the water conditions of the disc, which affirms the robustness of the approach.

The results thus achieved are very comparable between the two calibration curves, and the difference between the two water content estimates is usually in the range of 1.5% to 2.5%. Even in discs of very degenerated states, such as T10-T11 and T11-T12, the difference between the two estimates is small. This means that the two calibration curves can be considered acceptable and reliable for quantitative water content analysis, neither of which is lacking in relation to influencing the physiological interpretation of the result. For degenerated discs, it is found that the estimated water content for T10-T11 is 68.02% using the Marinelli curve and

67.14% using the combined curve, and for T11-T12 the values are 69.91% and 68.51% respectively. These values are entirely consistent with the values found in the literature in cases of advanced degeneration of discs. Particularly, Chiu et al. (2001) reports that in degenerated discs there is decreased water content to below 70%, whereas Zhu et al. (2018), using human disc simulations, shows loss of water content by 15-20% compared to physiological levels.

For the discs considered to be healthy or lightly degenerated, the estimates were more than 84%. The disc at T9-T10 exhibited a water content of 85.7% when the Marinelli curve was applied and 84.6% when the combined curve was applied, and for the disc at T12-L1, the estimates were 86.8% using the first curve and 85.34% using the second. These figures are entirely within the reported literature of human intervertebral discs' physiological ranges. While, according to the literature, the physiological water content of the healthy human intervertebral disc is normally 73% to 86% for the nucleus pulposus, and 65% to 75% for the annulus fibrosus (Newell et al., 2017; Antoniou et al., 1996). The results obtained in the present study are therefore fully within the physiological range of non-degenerated discs as would normally be expected.

In conclusion, the calculated water content values are in concordance with those reported in the literature for degenerated and healthy discs. The use of two independent calibration curves gave a more robust and confident estimation, adding strength to the validity of the method herein presented and to the strong basis for the subsequent mechanical property assignment in the finite element model.

3.3 Results and discussions of materials properties of nucleus.

In the present study, the elastic modulus and Poisson's coefficient of nucleus pulposus were estimated for segments T9-T10 and T12-L1. The estimation was done from the water content, which was calculated from two different calibration curves obtained from the literature. The elastic modulus values were calculated in relation of %W.C., while the Poisson's coefficient was subsequently calculated using a mathematical equation involving the elastic modulus. This procedure provided two sets of values for each parameter, allowing comparison of the two estimation methods. The result for elastic modulus of the nucleus pulposus agrees perfectly between the two curves. For T9-T10, we obtain 1.47 MPa with the combined curve and 1.31 MPa with the Marinelli curve; for T12-L1, we obtain 1.72 MPa and 1.45 MPa, respectively. These values are in the higher part of the reported physiological range for the human nucleus pulposus, which, according to various studies [59], [61], [77], usually ranges from 0.1 MPa to 2 MPa, depending on the model adopted. These values increase due to the high-water content of the nucleus considered, which is greater than 74% (Table 13).

Table 13: elastic modulus results

Nucleus	*%W.C. (Marinelli et al. 2009)*	*Elastic modulus (Marinelli et al. 2009)*	*%W.C (Marinelli 2009 with Weidenbaum 1992)*	*Elastic modulus (Marinelli 2009 with Weidenbaum 1992)*
T9/T10	79.46%	1.31 MPa	77.15%	1.47MPa
T12/L1	77.45%	1.45MPa	74.04%	1.72MPa

The graph in *Figure 48* provides visual support for the relationship between water content and estimated elastic modulus of the nucleus pulposus. There is a trend towards inverse correlation: greater water content is matched by reduced stiffness, as would be predicted for hydrated soft tissue biomechanics. Importantly, although the two calibration methods provide different absolute values, they both provide the same classification between segments, with T9/T10 softer than T12/L1.

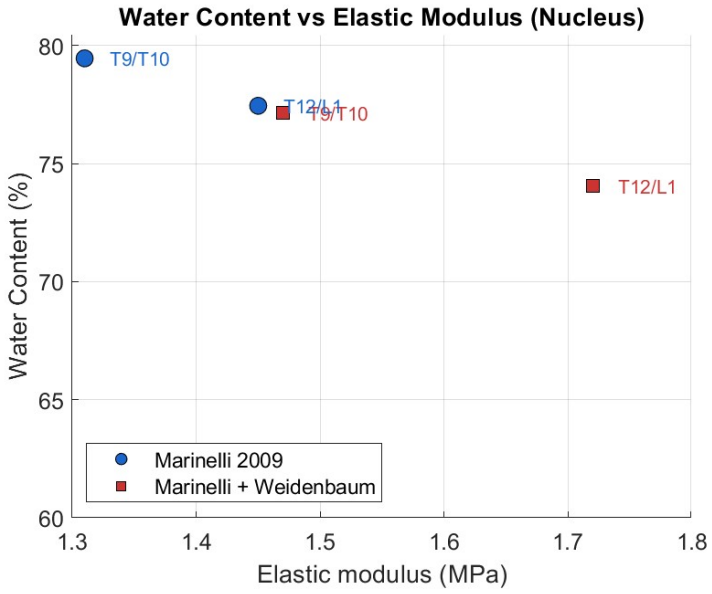

Figure 48:scatter plot of elastic modulus vs water content

The plot of *Figure 49*, representing the elastic modulus as a function of relaxation time T2, also shows behaviour according to the initial assumptions: higher values of T2 (corresponding to a higher proportion of water) are associated with lower elastic modulus. More specifically, T9/T10 is located at the lower right of the graph, with the highest relaxation time (~91.9 ms) and the lowest elastic modulus (1.31 MPa), while T12/L1 is vice versa. This response also attests to the sufficiency of the process of estimation employed, with the finding being that the T2 relaxation times obtained from MRI images can be adequately utilized as indicators of mechanical behaviour of the nucleus pulposus.

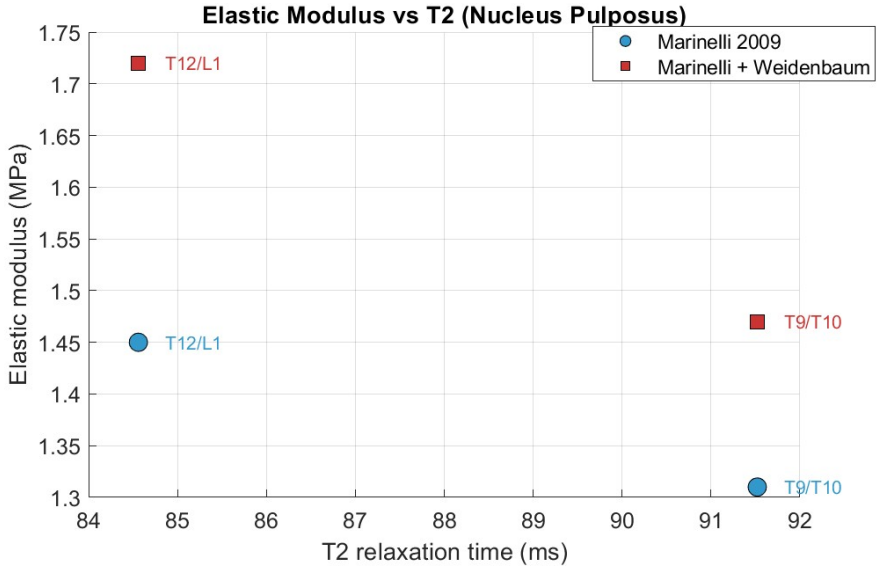

Figure 49 scatter plot of elastic modulus vs T2 time

In relation to Poisson's coefficient calculated from the elastic modulus, the following values are reached: 0.498 (T9-T10) and 0.490 (T12-L1) for the combined curve; 0.498 (T9-T10) and 0.4918 (T12-L1) for the Marinelli curve. The values are almost identical in the two curves and are in the upper range of the physiological range of the nucleus pulposus, usually 0.3 to 0.5 [78], [79]. The value of 0.5 is physiologically acceptable in highly hydrated tissue and represents high incompressibility, characteristic of normal nucleus pulposus (Table14-15).

Table 14: Poisson's rate from Marinelli data

Nucleus	*%H.L.*	*Compressibility (B)*	*Elastic modulus*	*Poisson's rate*
T9/T10	Healthy (0%)	$0.0065\frac{mm^2}{N}$	1.31 MPa	0.498
T12/L1	Moderate (15%)	$0.0335\frac{mm^2}{N}$	1.45MPa	0.4918

Table15: Poisson's rate from Marinelli and weidnabuer data

Nucleus	*%H.L.*	*Compressibility (B)*	*Elastic modulus*	*Poisson's rate*
T9/T10	Healthy (0%)	$0.0065\frac{mm^2}{N}$	1.47MPa	0.498
T12/L1	Moderate (15%)	$0.0335\frac{mm^2}{N}$	1.72MPa	0.490

Although two different calibration curves were employed to calculate the water content - and consequently two different methods for the determination of the elastic modulus - Poisson's ratio values proved to be very close to one another with slight differences. This similarity reflects that even though there is a minor variation in the estimation of elastic modulus, the theoretical relationship used in the calculation of the Poisson's ratio remains stable and consistent. That is, the computed results are within the range of possible values of hydrated disc tissues confirming that the nucleus pulposus, even with moderate degeneration, maintains a mechanical behaviour in accordance with its hydraulic nature. This observation validates the approach adopted for the mechanical characterization of the tissue to be right and suggests that the approach followed based on calibration curves derived from images and literature can be considered robust and repeatable even in slightly different environments.

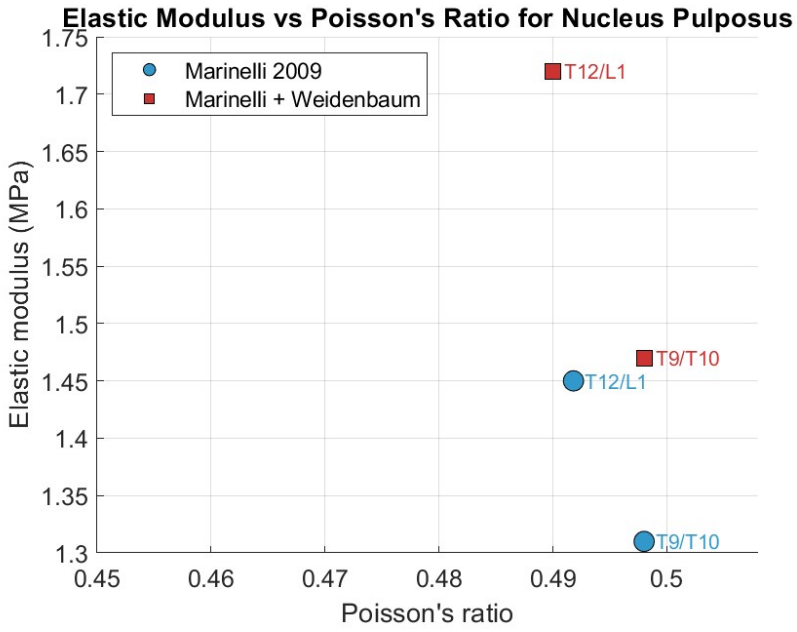

Figure 50: results of Poisson's rate related to elastic modulus

The figure for *Figure 50* represents the elastic modulus as a function of Poisson's coefficient for each nucleus and estimation approach. The distribution of the points easily shows that high values of the elastic modulus are linked to small decreases of the Poisson's coefficient. As an example, the point for segment T9-T10 with the Marinelli curve (blue circle) is at the bottom right, which means a less rigid material. On the other hand, the T12-L1 point with the curve of combined data (red square) represents the largest value of elastic modulus and a moderate decrease in the Poisson's coefficient. This phenomenon agrees with the biomechanical hypothesis that reduced water content (which is associated with degeneration) creates higher stiffness and smaller ability of transverse deformation. It is therefore confirmed that the technique applied can replicate pathophysiological changes of the mechanical characteristics of the nucleus pulposus. From the biomechanical point of view, these values are consistent with well-established behaviour of the nucleus. With greater water content, there is greater deformability (lower modulus of elasticity) and Poisson's coefficient, indicating that the fabric tends to expand greatly laterally on compression. This type of behaviour is typical of a fabric that can also function as a cushion and offer hydraulic function, like that of the nucleus pulposus.

In conclusion, the estimated nucleus pulposus parameters, based on two calibrating curves, are physiologically valid, biomechanically consistent and fully concordant with the reported values

in the literature. The approach adopted appears to be reproducible and precise for the calculation of mechanical properties in finite element analysis tailored models.

3.4 Results and discussions of materials properties of annulus.

In the present study, annulus fibrosus was modelled as a hyperelastic material using the three-parameter Mooney-Rivlin model. The parameter values C1 and C2 were specified in terms of the percentage of disc height loss (%HL), which was used as an indicator of tissue degeneration severity. The calibration curve was constructed based on combining data from various sources in the literature, that describe how degeneration affects the nonlinear mechanical properties of the annulus [58], [61], [62], [66].

One of the most significant methodological choices was modelling the T10-T11 and T11-T12 discs as intact annulus fibrosus. The choice to make this modelling decision came after the loss of morphological definition between nucleus and annulus seen, on the MRI scans, in strongly degenerated discs having a disorganized internal structure and no anatomical margins. The same condition is described in the literature as showing that, in the case of severe degeneration, the nucleus exhibits mechanical properties that can be matched with those of the annulus [64], [65], [77].

The calculated C1 and C2 values rise evidently with height loss. The values in non-degenerated disc (T9–T10), are low at around 0.21 MPa and 0.06 MPa, respectively. For moderately degenerated discs (T12–L1), the values rise to around 0.41 MPa and 0.10 MPa, respectively. In the most degenerate discs (T10–T11 and T11–T12), these values are 0.98 MPa for C1 and 0.25 MPa for C2 (Table 17).

Table 14: C1 and C2 parameters

Structure	*Height value*	*Normal height* [7]	*%H.L.*	*C1*	*C2*
AF T9/T10	4.989 mm	4.90mm	0%	0.2095	0.0519
IVD T10/T11	2.761mm	6.50mm	57.52%	0.9799	0.2495
IVD T11/T12	2.939mm	5.40mm	47.40%	0.8463	0.2153
AF T12/L1	5.730mm	6.80mm	15%	0.4103	0.1034

This is in line with the trend reported by Ruberté et al. (2009) [61], who showed that, as degeneration increases, annulus tissue loses its ability to deform and becomes stiffer. This behaviour is experimentally confirmed by Cai et al. (2020) [62] and Du et al. (2021) [58], who demonstrate fibrous thickening of the matrix and de-hydration loss leading to increase non-linear strength of the tissue. From the biomechanical perspective, the values obtained are within

the ranges of reported human annulus physiological values. Specifically, C1 is in the 0.1 MPa to 1 MPa range, and C2 is typically in the 0.05 MPa to 0.3 MPa range, depending on the level of degeneration. The identical trend observed in this study for %HL confirms that the calibration is accurate, and the computed parameters provide realistic depiction of loss of elasticity in a progressive fashion and increasing tissue stiffness.

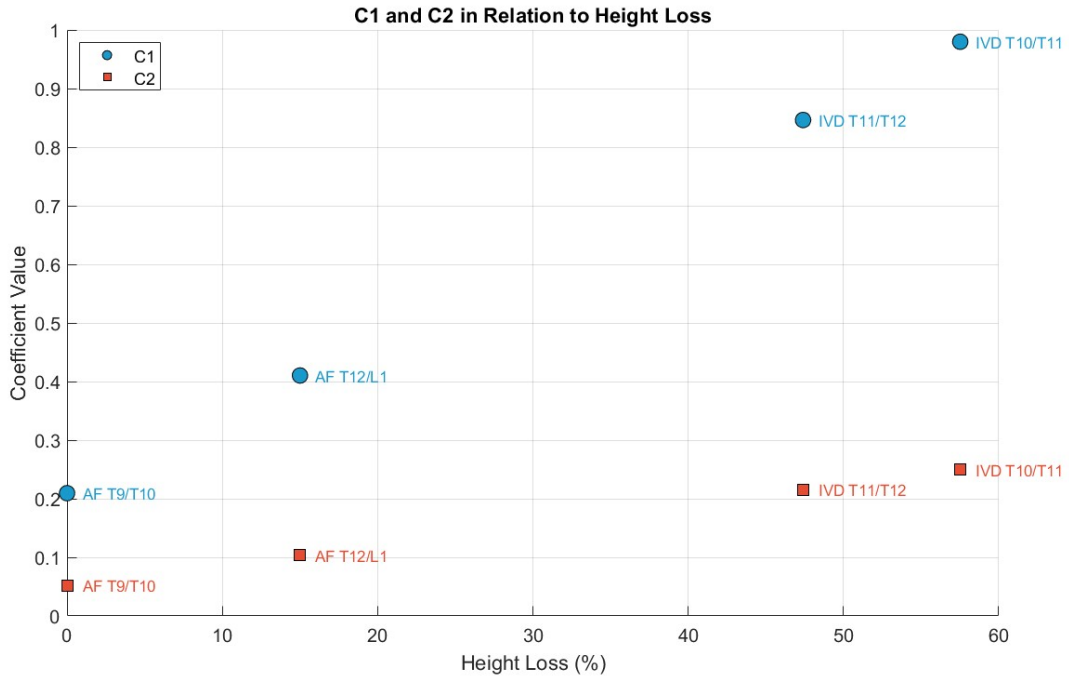

Figure 51: results of C1 and C2

Visual observation of the data within the graph is an additional proof of the authenticity of the calibration technique. The graph (Figure 51) well shows a linear and progressive rise in the C1 and C2 coefficients as a percentage disc height loss (%HL) function, with a very significant increase in the most degenerated discs (T10-T11 and T11-T12). Of great interest is the location of the structures with intact annulus, for example, T9-T10 and T12-L1, in the lower left quadrant of the figure, with correspondingly low values of both %HL and mechanical coefficients, which indicates a still intact elastic behaviour. In contrast, the completely degenerated discs, in which the nucleus and annulus have been modelled as a single hyperelastic material, are grouped together in the upper right-hand corner, with high stiffness parameters. This spatial division between healthy and degenerated disc illustrates the suitability of the application of %HL as a continuous metric of degeneration. Also, the monotonous and steady rise of the C1 and C2 values throughout the different samples is a testament to the internal

validity of the calibration and shows that the degenerative process influences the mechanical behaviour of the annulus in a measurable and predictable way.

Another consideration is the choice of parameter D, related to the compressibility of the material. For this study, the volume behaviour of the model was described by making the D term part of a three-parameter Mooney-Rivlin formulation. Unlike parameters C1 and C2, however, D was kept at the same constant value for all simulated discs regardless of their level of degeneration. This is corroborated by Rohlmann et al. (2006) [59], who, suggest that for a severely degenerated disc, compressibility can be assumed to be equal to that of the annulus. The authors explain that, at normal conditions, the compressibility of the nucleus is similar to water (0.0005 mm^2/N), but in degenerated discs increases to about 0.15 mm^2/N — the value assumed for the annulus fibrosus. Under this proposal, a constant value of D was assigned to annulus fibrosus independent of disc degeneration level. This is argued by the fact that, despite the tangential stiffness variation (defined by C1 and C2), compressibility of fibrous can be treated as a constant. Furthermore, correcting D allows the model to remain simplification yet remain very consistent biomechanically and without the addition of additional variables badly supported by the quantitative data currently available in the literature.

Overall, the approach of modelling the annulus fibrosus by assigning Mooney–Rivlin parameters by disc height loss was able to capture the increasing stiffness of the tissue with degeneration. The combination of literature data for calculating C1 and C2 from calibration curve combine with constant value for D, based on experimental observation, allowed us to develop a mechanically meaningful and physiologically applicable model.

3.5 Future Developments and Perspectives

The work presented in this thesis marks the first concrete step in the development of subject-specific biomechanical spine models based on the integration of CT and MRI scans. However, there are certain aspects that can be added upon to make this process even more complete and effective. The logical next step will be to conduct finite element simulations based on the research conducted already. Application of physiological or pathological loads to the model would enable consideration of stresses and deformations distribution of the discs and vertebrae, as well as the assessment of the given properties practically, and extending knowledge of the spinal biomechanics in terms of disc degeneration severity. Furthermore, the simulations would enable comparison with clinical or experimental evidence, thereby improving the validation of the model. A second potential development lies in enriching the anatomical model. At present, the interest is largely confined to the vertebrae and intervertebral discs, yet extension could include the incorporation of biomechanically significant structures like ligaments, facet joints, and paravertebral muscles. The addition of these structures would allow for the behaviour of the spinal column to be simulated more realistically, especially for complicated motions or pathological situations. In terms of materials, a future evolution might be to utilize more advanced constitutive models. While the hyperelastic Mooney-Rivlin model used for the annulus fibrosus was functional and computationally efficient choice, in the future, the adoption of anisotropic or poroelastic models that could more closely mimic the response of soft tissues may be considered. Though more complex, this type of modelling would also enable the viscoelastic properties and fluid flow in the disc to be simulated, which are fundamental characteristics, especially with advanced degeneration.

Chapter 4

Conclusion

The aim of this thesis was to create a three-dimensional, subject-specific model of the thoracolumbar spine through the integration of CT and MRI imaging. This enabled the realistic modelling of not only bone morphology, but also the intervertebral discs' functional and tissue properties. Compared with conventional models, which rely directly on CT images, this method offered non-invasive quantification of the key parameters, such as water content and mechanical properties, with particular emphasis laid on the nucleus and annulus. Through extensive segmentation, multimodal registration, and quantitative image analysis, an accurate model was reached wherein material properties were classified from subjective data gathered directly from images. Use of the Simulated Annealing algorithm for T2 relaxation time estimation and calibration curves from scientific literature allowed description of the biomechanical properties of the disc tissues in a compatible mode with their degenerative state. The experimental measurements thus obtained are consistent with published results both in terms of the level of the T2 and water content and in terms of the biomechanically estimated quantities, thereby justifying the proposed procedure. While the methodology presented here does not yet include the phase of finite element method (FEM) simulation, it presents a reliable foundation for further biomechanical and clinical studies, yielding an open process that can be used in different subjects.

In conclusion, this thesis has demonstrated that a high-fidelity, personalised biomechanical model of the spine can be constructed by the integration of data from different imaging modalities. This paves the way for the use of realistic models in research and the clinic with the potential of future applications to include numerical simulations and personalised applications and tools to support diagnosis and treatment planning.

Bibliography

[1] 'Anatomy of the Spine', Spinal Cord Injury Information Pages. Accessed: Jun. 01, 2025. [Online]. Available: https://www.sci-info-pages.com/anatomy-of-the-spine/

[2] F. H. Martini, R. B. Tallitsch, and J. L. Nath, *Anatomia umana*, 7. ed. / revisione a cura di Lucio Cocco ... [et al.]. Napoli: EdiSES, 2019.

[3] *Anatomy Bag Plus: Trattato di anatomia umana-Anatomia topografica-Atlante di anatomia umana*. S l.: Edi. Ermes, 2021.

[4] 'Anatomy of the Spine', Globus Medical. Accessed: Jun. 01, 2025. [Online]. Available: https://www.globusmedical.com/patient-education-musculoskeletal-system-conditions/symptoms/anatomy-of-the-spine/

[5] 'Thoracic Vertebra - an overview | ScienceDirect Topics'. Accessed: Jun. 01, 2025. [Online]. Available: https://www.sciencedirect.com/topics/medicine-and-dentistry/thoracic-vertebra

[6] G. Gkasdaris, G. Tripsianis, K. Kotopoulos, and S. Kapetanakis, 'Clinical anatomy and significance of the thoracic intervertebral foramen: A cadaveric study and review of the literature', *J. Craniovertebral Junction Spine*, vol. 7, no. 4, p. 228, 2016, doi: 10.4103/0974-8237.193266.

[7] B. A. Frost, S. Camarero-Espinosa, and E. J. Foster, 'Materials for the Spine: Anatomy, Problems, and Solutions', *Materials*, vol. 12, no. 2, p. 253, Jan. 2019, doi: 10.3390/ma12020253.

[8] *Manuale di ortopedia e traumatologia*, Seconda edizione. Milano: EDRA, 2016.

[9] 'Lumbar Vertebrae', Physiopedia. Accessed: Jun. 01, 2025. [Online]. Available: https://www.physio-pedia.com/Lumbar_Vertebrae

[10] N. Newell, J. Little, A. Christou, M. Adams, C. Adam, and S. Masouros, 'Biomechanics of the human intervertebral disc: A review of testing techniques and results', *J. Mech. Behav. Biomed. Mater.*, vol. 69, pp. 420–434, May 2017, doi: 10.1016/j.jmbbm.2017.01.037.

[11] P. P. Raj, 'Intervertebral Disc: Anatomy-Physiology-Pathophysiology-Treatment', *Pain Pract.*, vol. 8, no. 1, pp. 18–44, Jan. 2008, doi: 10.1111/j.1533-2500.2007.00171.x.

[12] 'Intervertebral disc', *Wikipedia*. Mar. 22, 2025. Accessed: Jun. 01, 2025. [Online]. Available: https://en.wikipedia.org/w/index.php?title=Intervertebral_disc&oldid=1281754880

[13] G. M. Jensen, 'Biomechanics of the Lumbar Intervertebral Disk: A Review', *Phys. Ther.*, vol. 60, no. 6, pp. 765–773, Jun. 1980, doi: 10.1093/ptj/60.6.765.

[14] A. Baldit, 'Micromechanics of the Intervertebral Disk', in *Multiscale Biomechanics*, Elsevier, 2018, pp. 455–467. doi: 10.1016/B978-1-78548-208-3.50011-3.

[15] M. Al-Abbasi, A.-J. F. Al-Rubai, and M. H. Assi, 'Quantification of the Water Content of Human Intervertebral Discs in Various Regions and Conditions', *Al-Rafidain J. Med. Sci. ISSN 2789-3219*, vol. 6, no. 2, pp. 43–47, Apr. 2024, doi: 10.54133/ajms.v6i2.715.

[16] P. Ghosh, *The Biology of the Intervertebral Disc*, 1st ed. CRC Press, 2019. doi: 10.1201/9780429280344.

[17] 'Material', Biomomentum. Accessed: Jun. 01, 2025. [Online]. Available: http://biomomentum.com

[18] F. Alonso and D. J. Hart, 'Intervertebral Disk', in *Encyclopedia of the Neurological Sciences*, Elsevier, 2014, pp. 724–729. doi: 10.1016/B978-0-12-385157-4.01154-4.

[19] P. Hadagali and S. Balasubramanian, 'Subject-specific finite element modeling of the adolescent thoracic spine for scoliosis research', Master of Science, Drexel University, Philadelphia, Pennsylvania, United States, 2014. doi: 10.17918/etd-6068.

[20] D. H. T. Spine and R. Group, 'Thoracic Degenerative Disc Disease NJ & NYC', Spine & Rehab Group. Accessed: Jun. 01, 2025. [Online]. Available: https://www.thespineandrehabgroup.com/thoracic-degenerative-disc-disease

[21] A. A. Elfadle, C. A. Zarad, A. A. A. Elmaaty, B. F. A. El-Nagaa, and A. Y. Soliman, 'Correlation between lumbar spinal canal magnetic resonance imaging grading systems and parameters in lumbar spinal canal compromise', *Egypt. J. Neurol. Psychiatry Neurosurg.*, vol. 58, no. 1, p. 104, Sep. 2022, doi: 10.1186/s41983-022-00543-0.

[22] M. A. O'Reilly and C. M. Whyne, 'Comparison of Computed Tomography Based Parametric and Patient-Specific Finite Element Models of the Healthy and Metastatic Spine Using a Mesh-Morphing Algorithm':, *Spine*, vol. 33, no. 17, pp. 1876–1881, Aug. 2008, doi: 10.1097/BRS.0b013e31817d9ce5.

[23] S. Kirnaz *et al.*, 'Pathomechanism and Biomechanics of Degenerative Disc Disease: Features of Healthy and Degenerated Discs', *Int. J. Spine Surg.*, vol. 15, no. s1, pp. 10–25, Apr. 2021, doi: 10.14444/8052.

[24] E. Dall'Ara, D. Pahr, P. Varga, F. Kainberger, and P. Zysset, 'QCT-based finite element models predict human vertebral strength in vitro significantly better than simulated DEXA', *Osteoporos. Int.*, vol. 23, no. 2, pp. 563–572, Feb. 2012, doi: 10.1007/s00198-011-1568-3.

[25] B. Weisse, A. K. Aiyangar, Ch. Affolter, R. Gander, G. P. Terrasi, and H. Ploeg, 'Determination of the translational and rotational stiffnesses of an L4–L5 functional spinal unit using a specimen-specific finite element model', *J. Mech. Behav. Biomed. Mater.*, vol. 13, pp. 45–61, Sep. 2012, doi: 10.1016/j.jmbbm.2012.04.002.

[26] P. Gao, 'Inverse Model of Human Lumbar Spine Based on CT Image and Finite Element Analysis', *Radioelectron. Commun. Syst.*, vol. 63, no. 6, pp. 319–327, Jun. 2020, doi: 10.3103/S0735272720060059.

[27] M. Turbucz *et al.*, 'Development and Validation of Two Intact Lumbar Spine Finite Element Models for In Silico Investigations: Comparison of the Bone Modelling Approaches', *Appl. Sci.*, vol. 12, no. 20, p. 10256, Oct. 2022, doi: 10.3390/app122010256.

[28] H. Du *et al.*, 'Biomechanical analysis of press-extension technique on degenerative lumbar with disc herniation and staggered facet joint', *Saudi Pharm. J.*, vol. 24, no. 3, pp. 305–311, May 2016, doi: 10.1016/j.jsps.2016.04.002.

[29] A. P. G. Castro and J. L. Alves, 'Numerical implementation of an osmo-poro-visco-hyperelastic finite element solver: application to the intervertebral disc', *Comput. Methods Biomech. Biomed. Engin.*, vol. 24, no. 5, pp. 538–550, Apr. 2021, doi: 10.1080/10255842.2020.1839059.

[30] B. T. Allaire *et al.*, 'Prediction of incident vertebral fracture using CT-based finite element analysis', *Osteoporos. Int.*, vol. 30, no. 2, pp. 323–331, Feb. 2019, doi: 10.1007/s00198-018-4716-1.

[31] M. Liaskos, M. A. Savelonas, P. A. Asvestas, M. G. Lykissas, and G. K. Matsopoulos, 'Bimodal CT/MRI-Based Segmentation Method for Intervertebral Disc Boundary Extraction', *Information*, vol. 11, no. 9, p. 448, Sep. 2020, doi: 10.3390/info11090448.

[32] G. Li-Xin, L. Rui, and Z. Ming, 'Biomechanical and fluid flowing characteristics of intervertebral disc of lumbar spine predicted by poroelastic finite element method', *Acta Bioeng. Biomech. 022016 ISSN 1509-409X*, 2016, doi: 10.5277/ABB-00406-2015-02.

[33] M. A. Stadelmann *et al.*, 'Integrating MRI-based geometry, composition and fiber architecture in a finite element model of the human intervertebral disc', *J. Mech. Behav. Biomed. Mater.*, vol. 85, pp. 37–42, Sep. 2018, doi: 10.1016/j.jmbbm.2018.05.005.

[34] M. A. Chetoui, O. Boiron, M. Ghiss, A. Dogui, and V. Deplano, 'Assessment of intervertebral disc degeneration-related properties using finite element models based on $$\uprho _H$$ ρ H -weighted MRI data', *Biomech. Model. Mechanobiol.*, vol. 18, no. 1, pp. 17–28, Feb. 2019, doi: 10.1007/s10237-018-1064-1.

[35] A.-J. Ren, Y. Guo, S.-P. Tian, L.-J. Shi, and M.-H. Huang, 'MR Imaging of the Spine at 3.0T with T2-Weighted IDEAL Fast Recovery Fast Spin-Echo Technique', *Korean J. Radiol.*, vol. 13, no. 1, p. 44, 2012, doi: 10.3348/kjr.2012.13.1.44.

[36] B. A. Jung and M. Weigel, 'Spin echo magnetic resonance imaging', *J. Magn. Reson. Imaging*, vol. 37, no. 4, pp. 805–817, Apr. 2013, doi: 10.1002/jmri.24068.

[37] H. Takashima *et al.*, 'Correlation between T2 relaxation time and intervertebral disk degeneration', *Skeletal Radiol.*, vol. 41, no. 2, pp. 163–167, Feb. 2012, doi: 10.1007/s00256-011-1144-0.

[38] C. P. L. Paul *et al.*, 'Quantitative MRI in early intervertebral disc degeneration: T1rho correlates better than T2 and ADC with biomechanics, histology and matrix content', *PLOS ONE*, vol. 13, no. 1, p. e0191442, Jan. 2018, doi: 10.1371/journal.pone.0191442.

[39] N. L. Marinelli, V. M. Haughton, and P. A. Anderson, 'T2 Relaxation Times Correlated with Stage of Lumbar Intervertebral Disk Degeneration and Patient Age', *Am. J. Neuroradiol.*, vol. 31, no. 7, pp. 1278–1282, Aug. 2010, doi: 10.3174/ajnr.A2080.

[40] X. Chen, X. Li, Y. Wang, and S. Lu, 'Relation of lumbar intervertebral disc height and severity of disc degeneration based on Pfirrmann scores', *Heliyon*, vol. 9, no. 10, p. e20764, Oct. 2023, doi: 10.1016/j.heliyon.2023.e20764.

[41] T. Çetin, S. Kahraman, V. Kızılgöz, and S. Aydın, 'The Comparison between Herniated and Non-Herniated Disc Levels Regarding Intervertebral Disc Space Height and Disc Degeneration, A Magnetic Resonance Study', *Diagnostics*, vol. 13, no. 20, p. 3190, Oct. 2023, doi: 10.3390/diagnostics13203190.

[42] N. Guellil *et al.*, 'Novel Methods to Measure Height and Volume in Healthy and Degenerated Lumbar Discs in MRIs: A Reliability Assessment Study', *Diagnostics*, vol. 12, no. 6, p. 1437, Jun. 2022, doi: 10.3390/diagnostics12061437.

[43] S. A. Nagy *et al.*, 'A Statistical Model for Intervertebral Disc Degeneration: Determination of the Optimal T2 Cut-Off Values', *Clin. Neuroradiol.*, vol. 24, no. 4, pp. 355–363, Dec. 2014, doi: 10.1007/s00062-013-0266-2.

[44] N. L. Marinelli, V. M. Haughton, A. Muñoz, and P. A. Anderson, 'T2 Relaxation Times of Intervertebral Disc Tissue Correlated With Water Content and Proteoglycan Content':, *Spine*, vol. 34, no. 5, pp. 520–524, Mar. 2009, doi: 10.1097/BRS.0b013e318195dd44.

[45] W. Y. Gu, X. G. Mao, R. J. Foster, M. Weidenbaum, V. C. Mow, and B. A. Rawlins, 'The Anisotropic Hydraulic Permeability of Human Lumbar Anulus Fibrosus: Influence of Age, Degeneration, Direction, and Water Content', *Spine*, vol. 24, no. 23, p. 2449, Dec. 1999, doi: 10.1097/00007632-199912010-00005.

[46] B. Yang, M. F. Wendland, and G. D. O'Connell, 'Direct Quantification of Intervertebral Disc Water Content Using MRI', *J. Magn. Reson. Imaging*, vol. 52, no. 4, pp. 1152–1162, Oct. 2020, doi: 10.1002/jmri.27171.

[47] J. Nazari, M. H. Pope, and R. A. Graveling, 'Feasibility of Magnetic resonance imaging (MRI) in obtaining nucleus pulposus (NP) water content with changing postures', *Magn. Reson. Imaging*, vol. 33, no. 4, pp. 459–464, May 2015, doi: 10.1016/j.mri.2015.01.006.

[48] M. Weidenbaum *et al.*, 'Correlating magnetic resonance imaging with the biochemical content of the normal human intervertebral disc', *J. Orthop. Res.*, vol. 10, no. 4, pp. 552–561, Jul. 1992, doi: 10.1002/jor.1100100410.

[49] N. L. Marinelli, V. M. Haughton, and P. A. Anderson, 'T2 Relaxation Times Correlated with Stage of Lumbar Intervertebral Disk Degeneration and Patient Age', *Am. J. Neuroradiol.*, vol. 31, no. 7, pp. 1278–1282, Aug. 2010, doi: 10.3174/ajnr.A2080.

[50] R. N. Natarajan, J. R. Williams, and G. B. J. Andersson, 'Modeling Changes in Intervertebral Disc Mechanics with Degeneration', *VO LU M E*.

[51] N. Boos, S. Weissbach, H. Rohrbach, C. Weiler, K. F. Spratt, and A. G. Nerlich, 'Classification of Age-Related Changes in Lumbar Intervertebral Discs'.

[52] J. P. G. Urban and C. P. Winlove, 'Pathophysiology of the intervertebral disc and the challenges for MRI', *J. Magn. Reson. Imaging*, vol. 25, no. 2, pp. 419–432, Feb. 2007, doi: 10.1002/jmri.20874.

[53] J. C. Iatridis, L. A. Setton, M. Weidenbaum, and V. C. Mow, 'Alterations in the mechanical behavior of the human lumbar nucleus pulposus with degeneration and aging', *J. Orthop. Res.*, vol. 15, no. 2, pp. 318–322, Mar. 1997, doi: 10.1002/jor.1100150224.

[54] M. Qasim, R. N. Natarajan, H. S. An, and G. B. J. Andersson, 'Damage accumulation location under cyclic loading in the lumbar disc shifts from inner annulus lamellae to peripheral annulus with increasing disc degeneration', *J. Biomech.*, vol. 47, no. 1, pp. 24–31, Jan. 2014, doi: 10.1016/j.jbiomech.2013.10.032.

[55] G. Li-Xin, L. Rui, and Z. Ming, 'Biomechanical and fluid flowing characteristics of intervertebral disc of lumbar spine predicted by poroelastic finite element method', *Acta Bioeng. Biomech. 022016 ISSN 1509-409X*, 2016, doi: 10.5277/ABB-00406-2015-02.

[56] W. Wilson, C. C. Van Donkelaar, and J. M. Huyghe, 'A Comparison Between Mechano-Electrochemical and Biphasic Swelling Theories for Soft Hydrated Tissues', *J. Biomech. Eng.*, vol. 127, no. 1, pp. 158–165, Feb. 2005, doi: 10.1115/1.1835361.

[57] W. M. Park, K. Kim, and Y. H. Kim, 'Effects of degenerated intervertebral discs on intersegmental rotations, intradiscal pressures, and facet joint forces of the whole lumbar spine', *Comput. Biol. Med.*, vol. 43, no. 9, pp. 1234–1240, Sep. 2013, doi: 10.1016/j.compbiomed.2013.06.011.

[58] C.-F. Du *et al.*, 'Does oblique lumbar interbody fusion promote adjacent degeneration in degenerative disc disease: A finite element analysis', *Comput. Biol. Med.*, vol. 128, p. 104122, Jan. 2021, doi: 10.1016/j.compbiomed.2020.104122.

[59] A. Rohlmann, T. Zander, H. Schmidt, H.-J. Wilke, and G. Bergmann, 'Analysis of the influence of disc degeneration on the mechanical behaviour of a lumbar motion segment using the finite element method', *J. Biomech.*, vol. 39, no. 13, pp. 2484–2490, Jan. 2006, doi: 10.1016/j.jbiomech.2005.07.026.

[60] B. Zhang, T.-C. Li, X. Wang, R. Zhu, C.-F. Du, and Y. Xie, 'The Effect of Disc Degeneration on the Biomechanical Response of the Lumbar Spine under Vibration Loading Condition', *J. Med. Biol. Eng.*, vol. 45, no. 1, pp. 22–33, Feb. 2025, doi: 10.1007/s40846-024-00921-4.

[61] L. M. Ruberté, R. N. Natarajan, and G. Bj. Andersson, 'Influence of single-level lumbar degenerative disc disease on the behavior of the adjacent segments—A finite element model study', *J. Biomech.*, vol. 42, no. 3, pp. 341–348, Feb. 2009, doi: 10.1016/j.jbiomech.2008.11.024.

[62] X. Cai *et al.*, 'Biomechanical Effect of L_4–L_5 Intervertebral Disc Degeneration on the Lower Lumbar Spine: A Finite Element Study', *Orthop. Surg.*, vol. 12, no. 3, pp. 917–930, Jun. 2020, doi: 10.1111/os.12703.

[63] X.-Y. Zhang and Y. Han, 'Comparison of the biomechanical effects of lumbar disc degeneration on normal patients and osteoporotic patients: A finite element analysis', *Med. Eng. Phys.*, vol. 112, p. 103952, Feb. 2023, doi: 10.1016/j.medengphy.2023.103952.

[64] N. D. Panagiotacopulos, M. H. Pope, R. Bloch, and M. H. Krag, 'Water Content in Human Intervertebral Discs: Part II. Viscoelastic Behavior', *Spine*, vol. 12, no. 9, pp. 918–924, Nov. 1987, doi: 10.1097/00007632-198711000-00013.

[65] H. Schmidt *et al.*, 'Application of a new calibration method for a three-dimensional finite element model of a human lumbar annulus fibrosus', *Clin. Biomech.*, vol. 21, no. 4, pp. 337–344, May 2006, doi: 10.1016/j.clinbiomech.2005.12.001.

[66] C. Liang, L. Yang, Y. Wang, J. Zhang, and B. Zhang, 'Development and validation of a human lumbar spine finite element model based on an automated process: Application to disc degeneration', *Biomed. Signal Process. Control*, vol. 105, p. 107547, Jul. 2025, doi: 10.1016/j.bspc.2025.107547.

[67] J. C. M. Teo *et al.*, 'Heterogeneous meshing and biomechanical modeling of human spine', *Med. Eng. Phys.*, vol. 29, no. 2, pp. 277–290, Mar. 2007, doi: 10.1016/j.medengphy.2006.02.012.

[68] M. A. O'Reilly and C. M. Whyne, 'Comparison of Computed Tomography Based Parametric and Patient-Specific Finite Element Models of the Healthy and Metastatic Spine Using a Mesh-Morphing Algorithm':, *Spine*, vol. 33, no. 17, pp. 1876–1881, Aug. 2008, doi: 10.1097/BRS.0b013e31817d9ce5.

[69] K. Nispel *et al.*, 'From MRI to FEM: an automated pipeline for biomechanical simulations of vertebrae and intervertebral discs', *Front. Bioeng. Biotechnol.*, vol. 12, p. 1485115, Jan. 2025, doi: 10.3389/fbioe.2024.1485115.

[70] A. C. Jones and R. K. Wilcox, 'Finite element analysis of the spine: Towards a framework of verification, validation and sensitivity analysis', *Med. Eng. Phys.*, vol. 30, no. 10, pp. 1287–1304, Dec. 2008, doi: 10.1016/j.medengphy.2008.09.006.

[71] Abhijeet Thorat and S. Chalipat, 'Use of Morphing Tool to Build Parametric Finite Element Vehicle Model', 2024, doi: 10.13140/RG.2.2.18813.78569.

[72] E. J. Chiu, D. C. Newitt, M. R. Segal, S. S. Hu, J. C. Lotz, and S. Majumdar, 'Magnetic Resonance Imaging Measurement of Relaxation and Water Diffusion in the Human Lumbar Intervertebral Disc Under Compression In Vitro':, *Spine*, vol. 26, no. 19, pp. E437–E444, Oct. 2001, doi: 10.1097/00007632-200110010-00017.

[73] R. N. Alkalay, D. Vader, and D. Hackney, 'The degenerative state of the intervertebral disk independently predicts the failure of human lumbar spine to high rate loading: An experimental study', *Clin. Biomech.*, vol. 30, no. 2, pp. 211–218, Feb. 2015, doi: 10.1016/j.clinbiomech.2014.09.016.

[74] M. Drake-Pérez *et al.*, 'Normal Values of Magnetic Relaxation Parameters of Spine Components with the Synthetic MRI Sequence', *Am. J. Neuroradiol.*, vol. 39, no. 4, pp. 788–795, Apr. 2018, doi: 10.3174/ajnr.A5566.

[75] S. Virk, K. N. Meyers, V. Lafage, S. A. Maher, and T. Chen, 'Analysis of the influence of species, intervertebral disc height and Pfirrmann classification on failure load of an injured disc using a novel disc herniation model', *Spine J.*, vol. 21, no. 4, pp. 698–707, Apr. 2021, doi: 10.1016/j.spinee.2020.10.030.

[76] Q. Zhu, X. Gao, M. D. Brown, H. T. Temple, and W. Gu, 'Simulation of water content distributions in degenerated human intervertebral discs', *J. Orthop. Res.*, vol. 35, no. 1, pp. 147–153, Jan. 2017, doi: 10.1002/jor.23284.

[77] N. Newell, D. Carpanen, G. Grigoriadis, J. P. Little, and S. D. Masouros, 'Material properties of human lumbar intervertebral discs across strain rates', *Spine J.*, vol. 19, no. 12, pp. 2013–2024, Dec. 2019, doi: 10.1016/j.spinee.2019.07.012.

[78] D. H. Cortes, N. T. Jacobs, J. F. DeLucca, and D. M. Elliott, 'Elastic, permeability and swelling properties of human intervertebral disc tissues: A benchmark for tissue engineering', *J. Biomech.*, vol. 47, no. 9, pp. 2088–2094, Jun. 2014, doi: 10.1016/j.jbiomech.2013.12.021.

[79] W.-H. Chuang *et al.*, 'Biomechanical Effects of Disc Degeneration and Hybrid Fixation on the Transition and Adjacent Lumbar Segments: Trade-off Between Junctional Problem, Motion Preservation, and Load Protection', *Spine*, vol. 37, no. 24, pp. E1488–E1497, Nov. 2012, doi: 10.1097/BRS.0b013e31826cdd93.